# Supplementary information: Alkali Metal Alkoxyborate Ester Salts; a Contemporary Look at Old Compounds

Amanda Berger[a], Ainee Ibrahim[a], Thomas A. Hales[a], Anita M. D'Angelo[b], Craig E. Buckley[a], Mark Paskevicius[a]*

[a]Department of Physics and Astronomy, Institute of Energy Transition, Curtin University, GPO Box U1987, Perth, WA 6845, Australia.

[b]Australian Synchrotron (ANSTO), 800 Blackburn Road Clayton VIC 3168

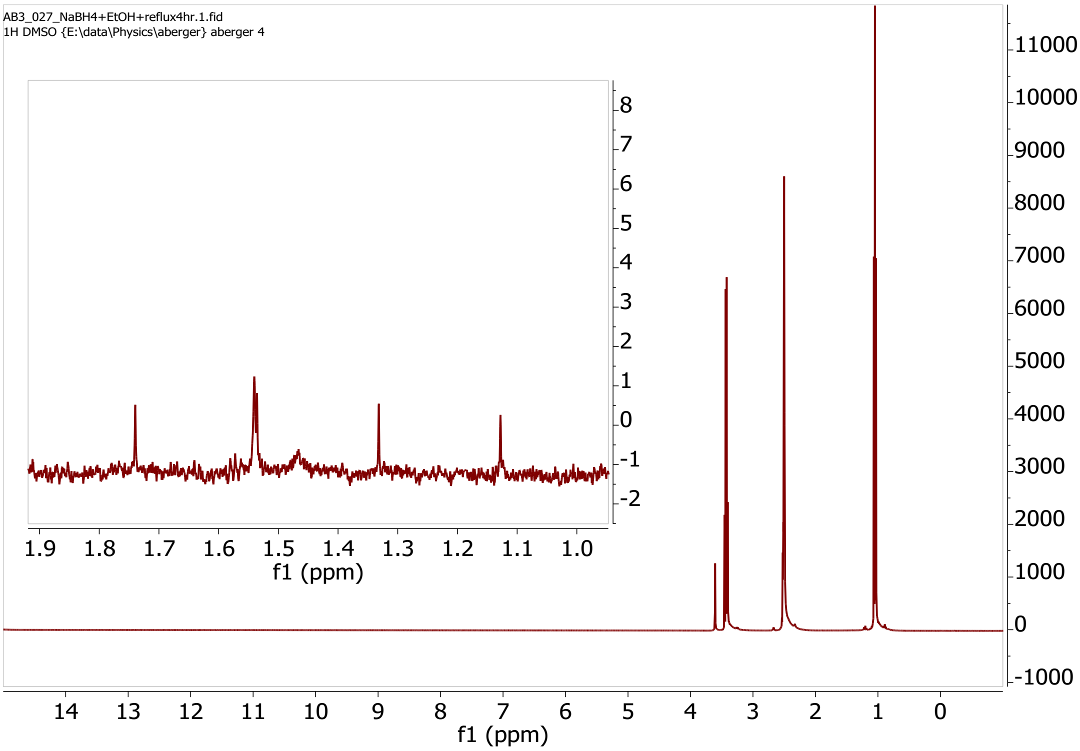


Figure S1: [1]H NMR of ethanolysis of $NaBH_4$ after 4 hours refluxing. Inset shows an expanded view indicating that $BH_4^-$ was still present in the final product with the 1:1:1:1 quartet of $BH_4^-$. Solvent DMSO-*d6*.

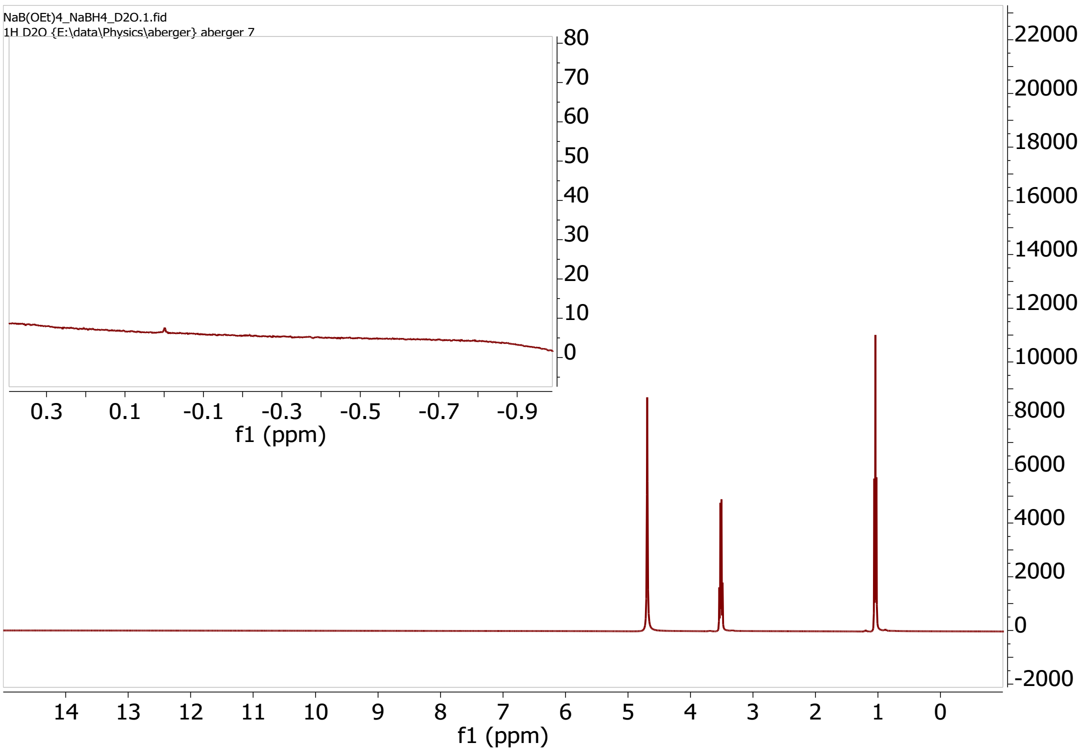


Figure S2: [1]H NMR of compound after 4.5 hours refluxing $NaBH_4$ in ethanol. Inset shows an expanded view indicating that no $BH_4^-$ was present in the final product with the 1:1:1:1 quartet of $BH_4^-$. Solvent $D_2O$.

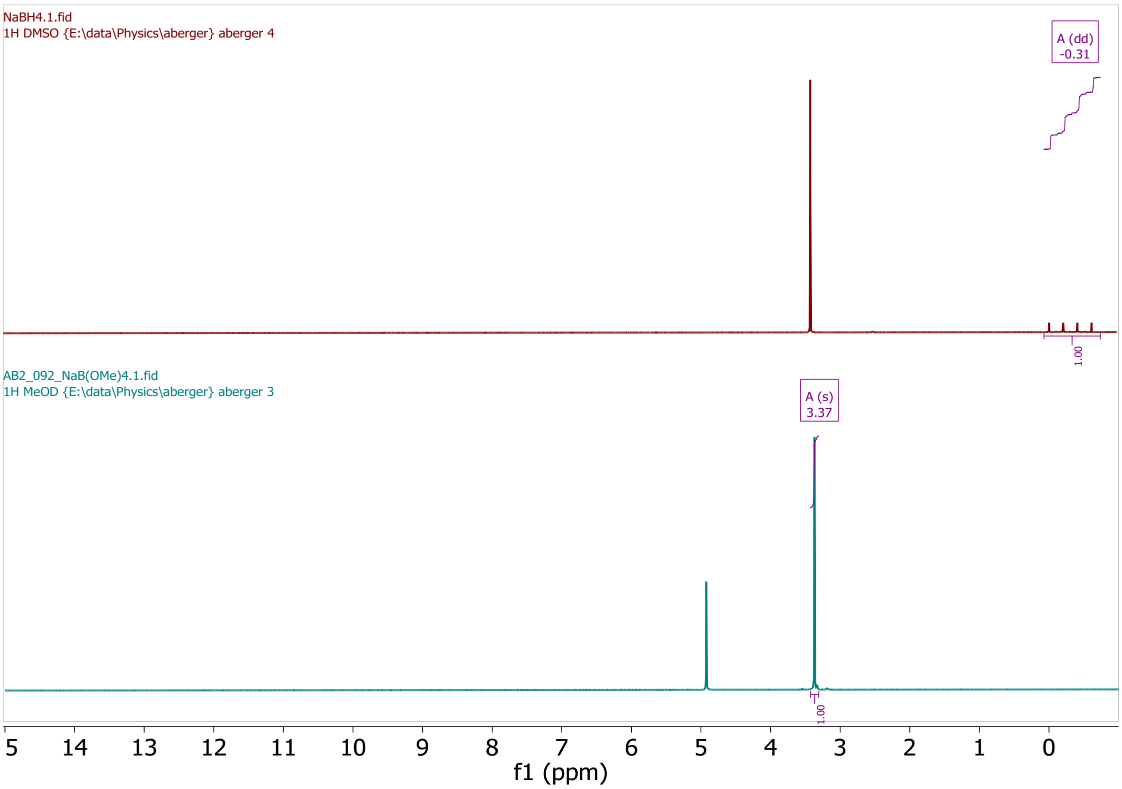


Figure S3: $^{1}H$ NMR of $NaBH_4$ (top) in DMSO-*d6* and (bottom) $Na[B(OMe)_4]$ in MeOD. The peak at 3.35 ppm in the $NaBH_4$ sample was caused by a contamination of water in the deuterated DMSO solvent. In the $Na[B(OMe)_4]$ $^{1}H$ NMR, the peak at 4.9 ppm was caused by water.

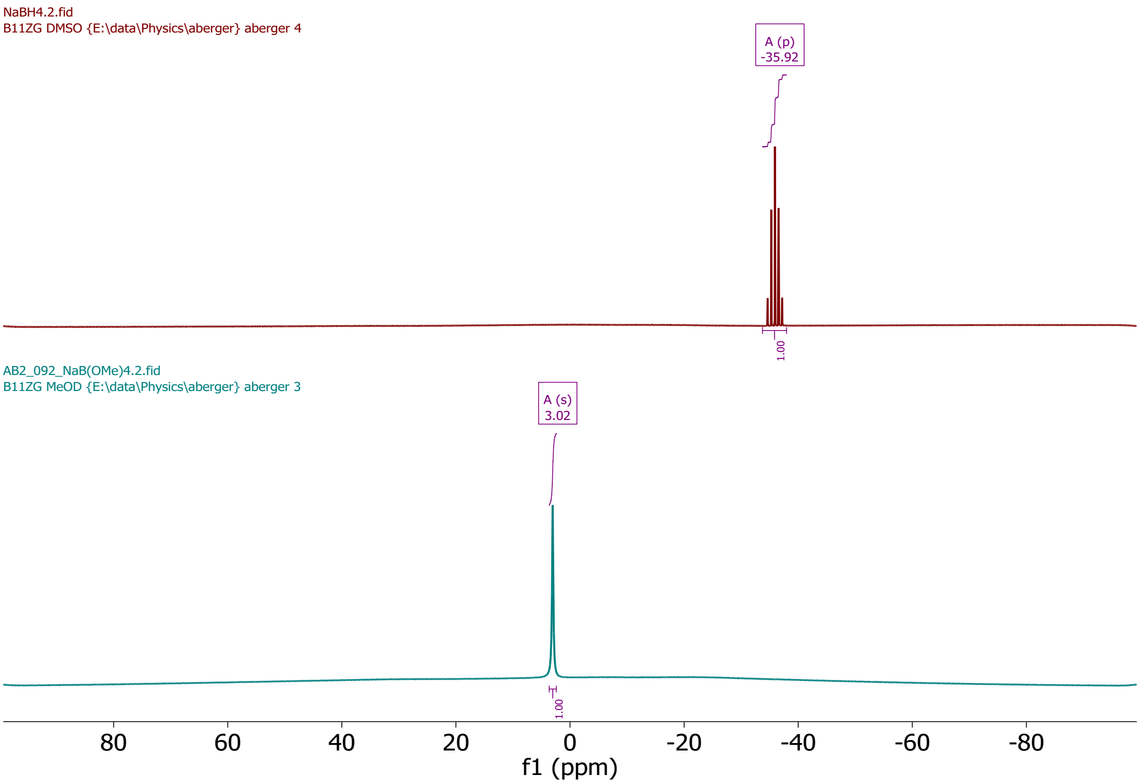


Figure S4: $^{11}B$ NMR of (top) $NaBH_4$ in DMSO-*d6* and (bottom) $Na[B(OMe)_4]$ in MeOD.

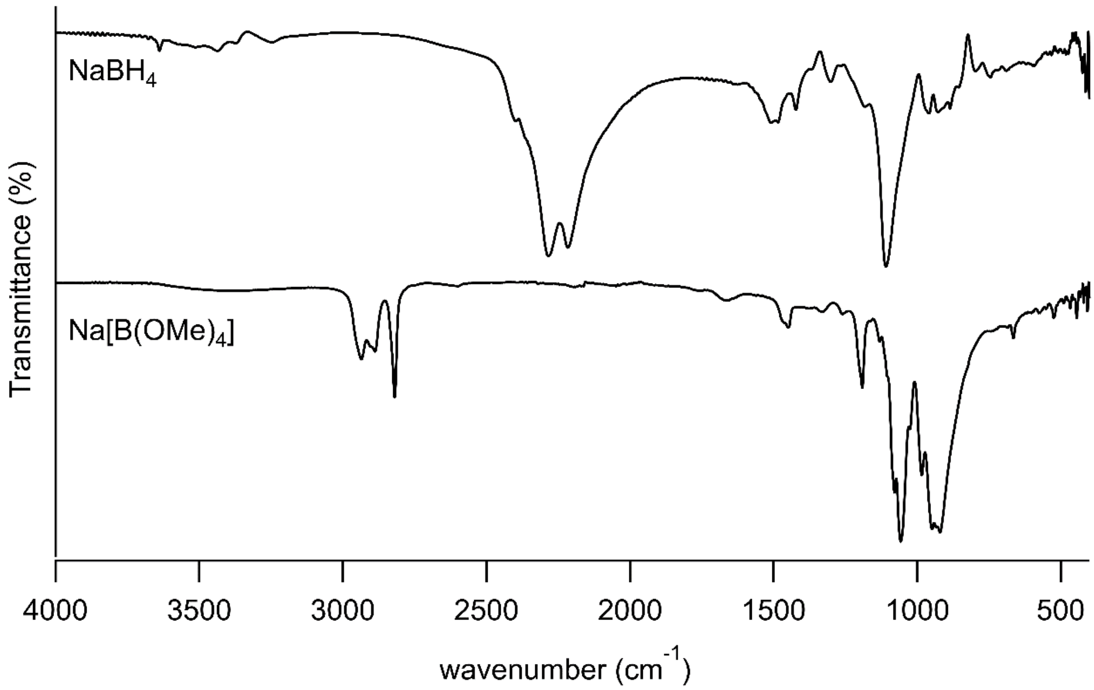


Figure S5: FTIR of $NaBH_4$ (top) and $Na[B(OMe)_4]$ (bottom).

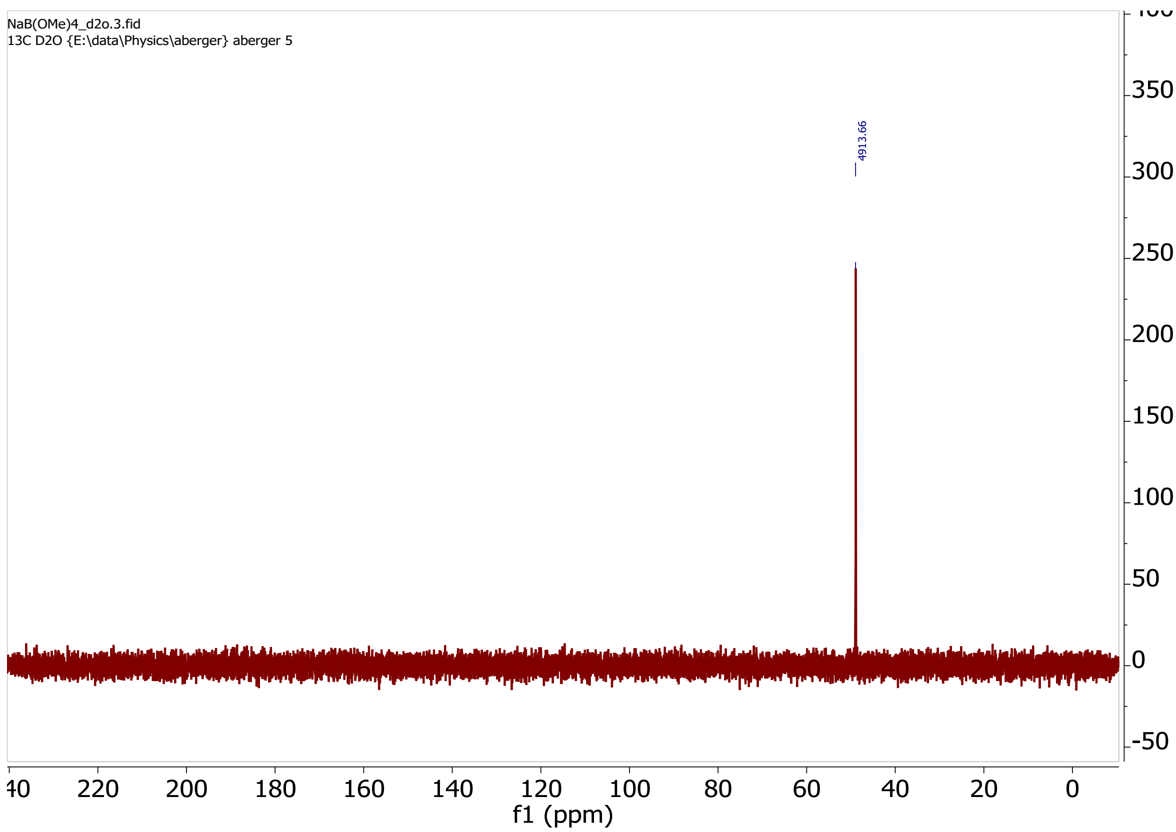


Figure S6: $^{13}C\{^{1}H\}$ NMR of $Na[B(OMe)_4]$ in $D_2O$.

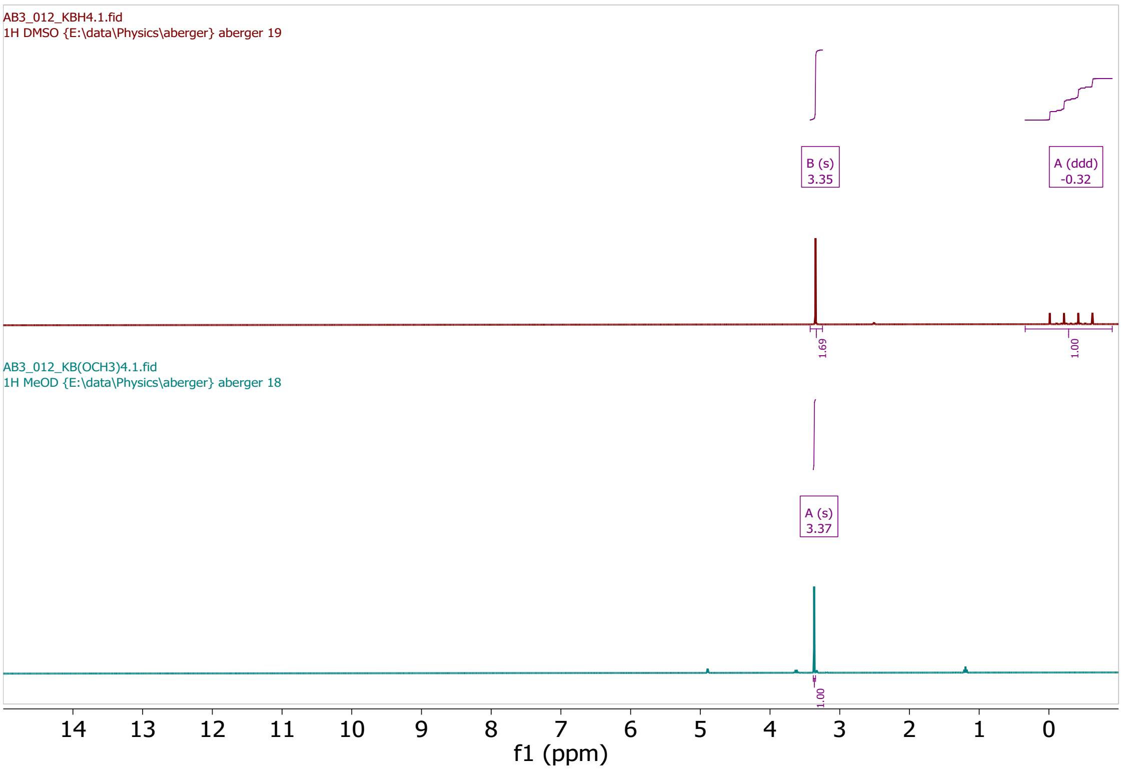


Figure S7: $^{1}H$ NMR of $KBH_4$ (top) in DMSO-*d6* and (bottom) $K[B(OMe)_4]$ in MeOD.

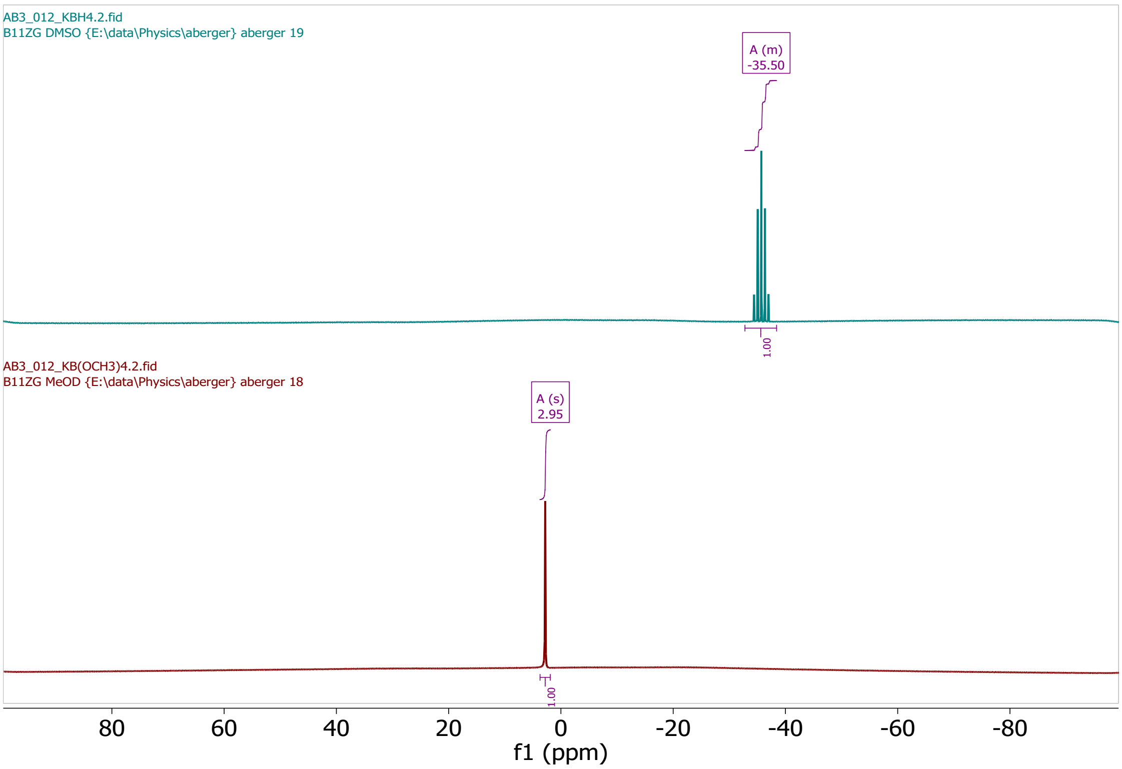


Figure S8: $^{11}B$ NMR of (top) $KBH_4$ in DMSO-*d6* and (bottom) $K[B(OMe)_4]$ in MeOD.

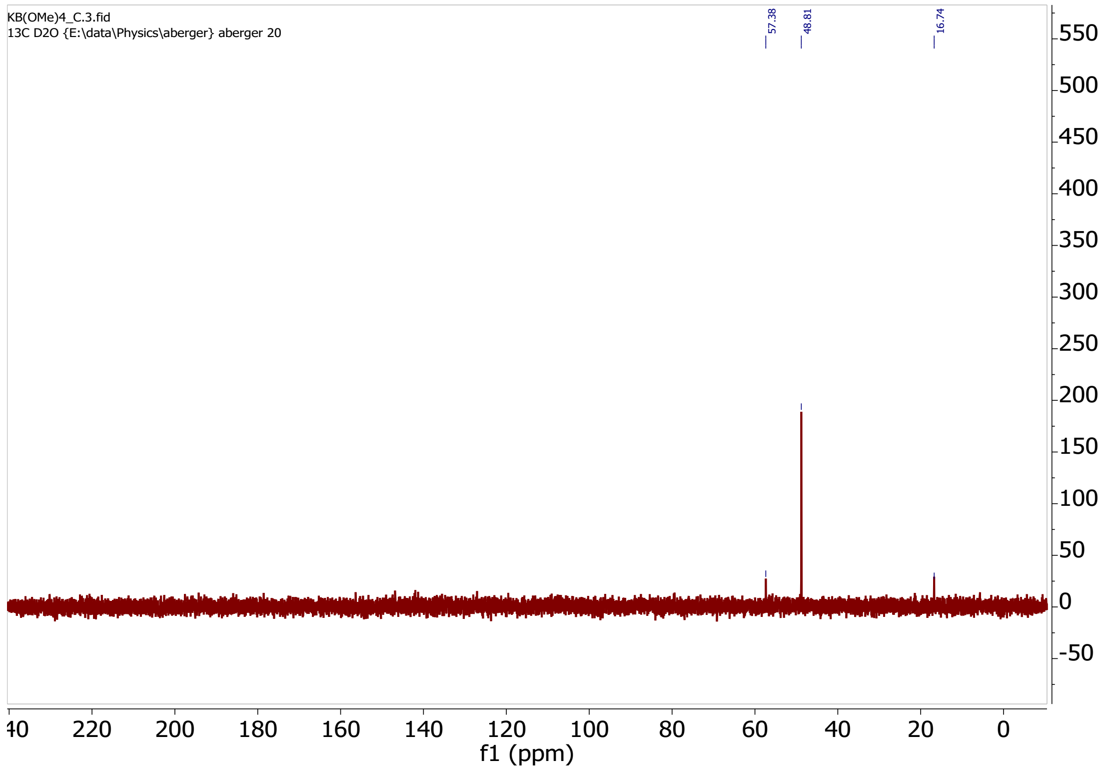


Figure S9: $^{13}C\{^{1}H\}$ NMR of $K[B(OMe)_4]$ in $D_2O$. There is a small contamination of ethanol due to the synthesis of $KBH_4$.

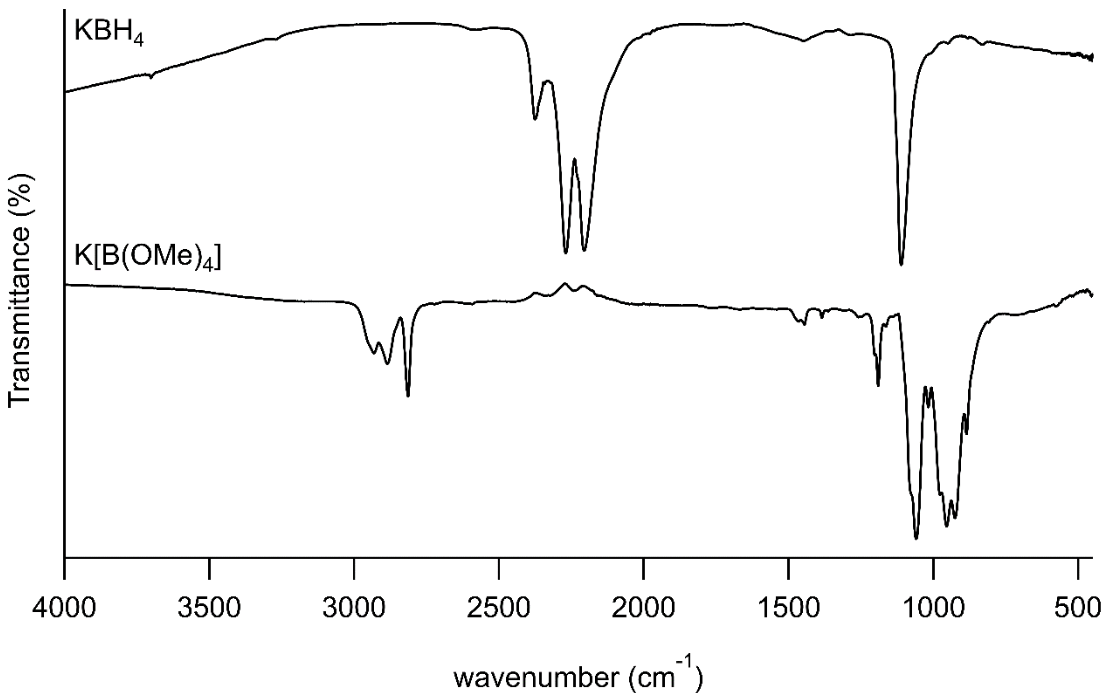


Figure S10: FTIR of $KBH_4$ (top) and $K[B(OMe)_4]$ (bottom).

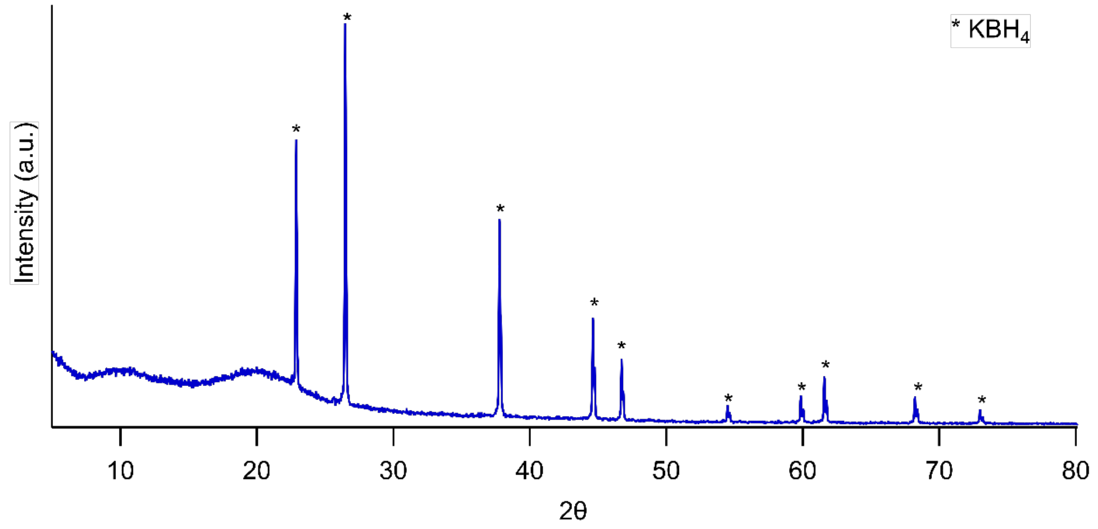


Figure S11: XRD of $KBH_4$. CuKα radiation, 1.54056 Å.

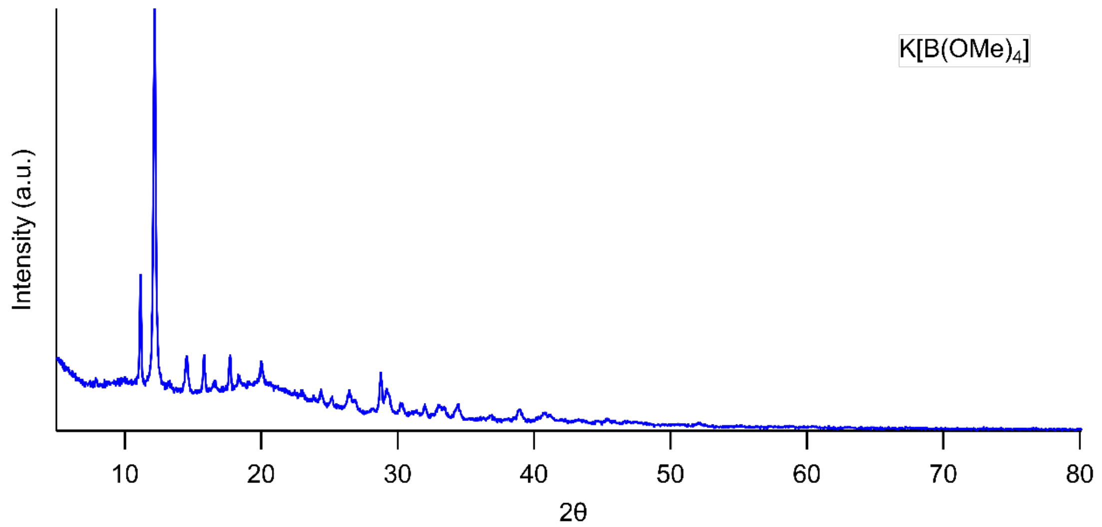


Figure S12: XRD of $K[B(OMe)_4]$. CuKα radiation, 1.54056 Å.

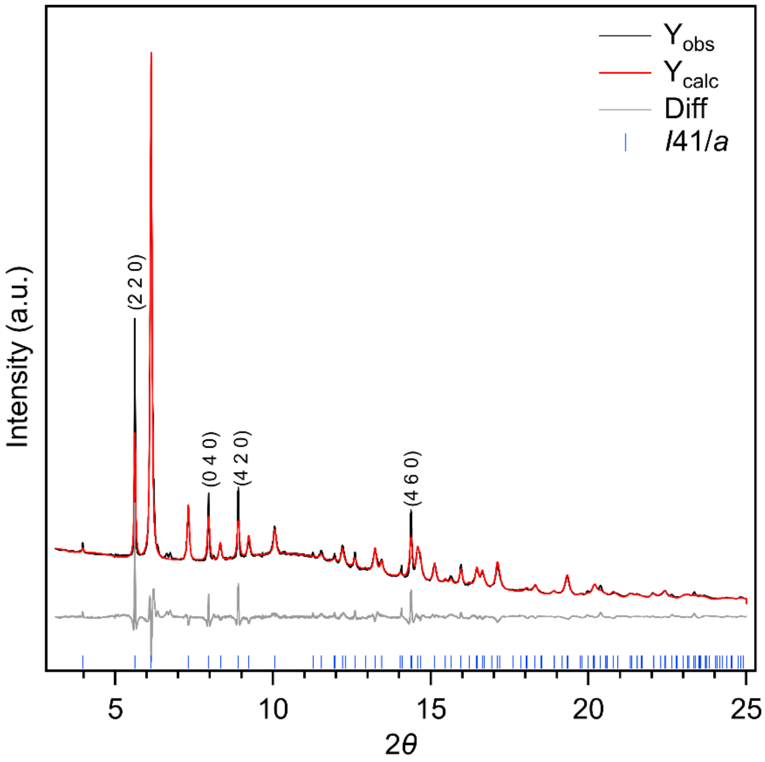


Figure S13: SR-XRD ($\lambda$ = 0.774863(1) Å) and Rietveld refinement of K[B(OMe)$_4$] at 25.5 °C. Experimental data as black line, calculated diffraction pattern as red line, and difference plot in grey. Blue tick marks represent Bragg positions from space group *I41/a*. Preferred orientation was observed along the labelled *hkl* indices due to the layered structure. Beam energy 16 keV ($\lambda$ = 0.774954(1) Å).

Table S1: Structural parameters for K[B(OMe)$_4$] at 25.5 °C ($a$ = 22.337(2) Å, $c$ = 7.648(3) Å, $V$ = 3815.6(4) Å$^3$, $\rho$ = 1.128(1) g/cm$^3$) in space group *I41/a* from TOPAS refinement of SR-XRD data, $R_{wp}$ = 4.769, All thermal parameters were fixed at $B_{iso}$ = 1.

| Name | Atom | Wyckoff | *x/a* | *y/b* | *z/c* |
|---|---|---|---|---|---|
| K1 | K | 16 | 0.5567(3) | 0.8038(3) | -0.2875(8) |
| O1 | O | 16 | -0.2144(2) | 0.5800(2) | -0.8093(7) |
| O2 | O | 16 | -0.1613(2) | 0.5515(2) | -0.5770(7) |
| O3 | O | 16 | -0.1672(2) | 0.6548(2) | -0.6324(7) |
| O4 | O | 16 | -0.1117(2) | 0.5862(2) | -0.8132(7) |
| B1 | B | 16 | -0.1638(2) | 0.5913(2) | -0.7080(7) |
| C1 | C | 16 | -0.2273(2) | 0.6075(2) | -0.9658(7) |
| C2 | C | 16 | -0.1259(2) | 0.5556(2) | -0.4204(7) |
| C3 | C | 16 | -0.2050(2) | 0.6666(2) | -0.5111(7) |

| | | | | | |
|---|---|---|---|---|---|
| C4 | C | 16 | -0.1045(2) | 0.5394(2) | -0.9183(7) |

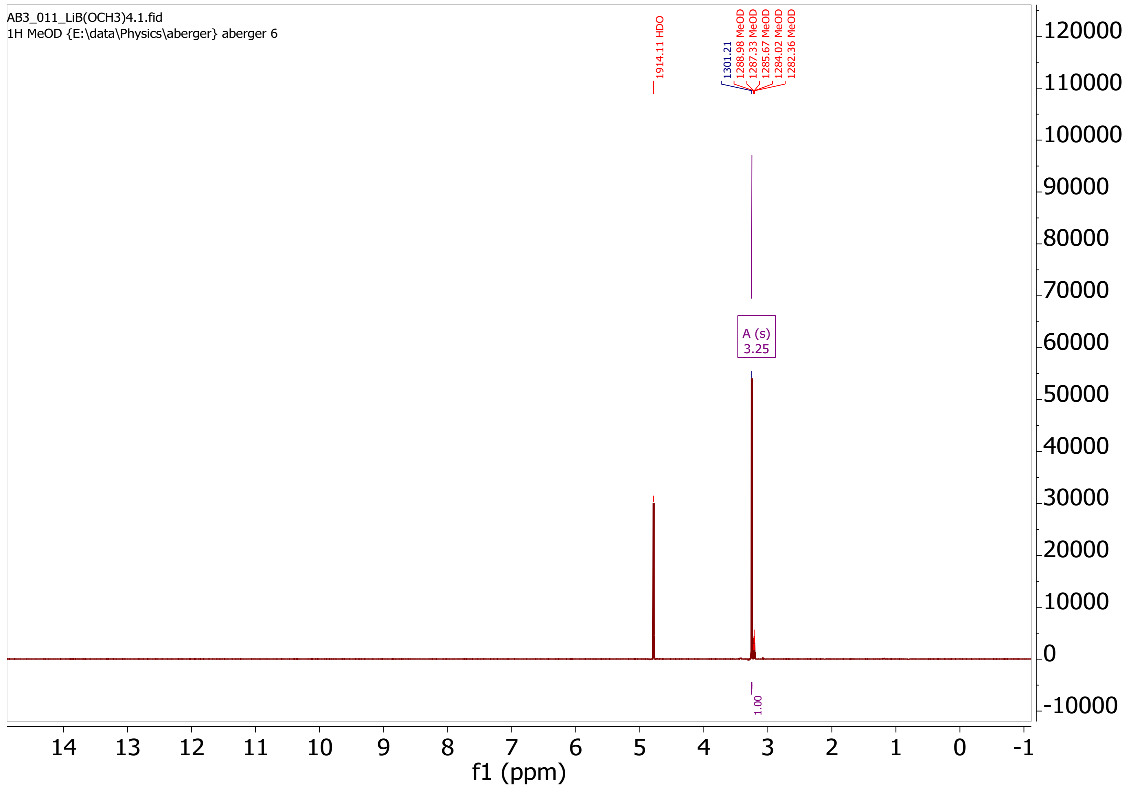


Figure S14: $^{1}H$ NMR of $Li[B(OMe)_4]$ in MeOD.

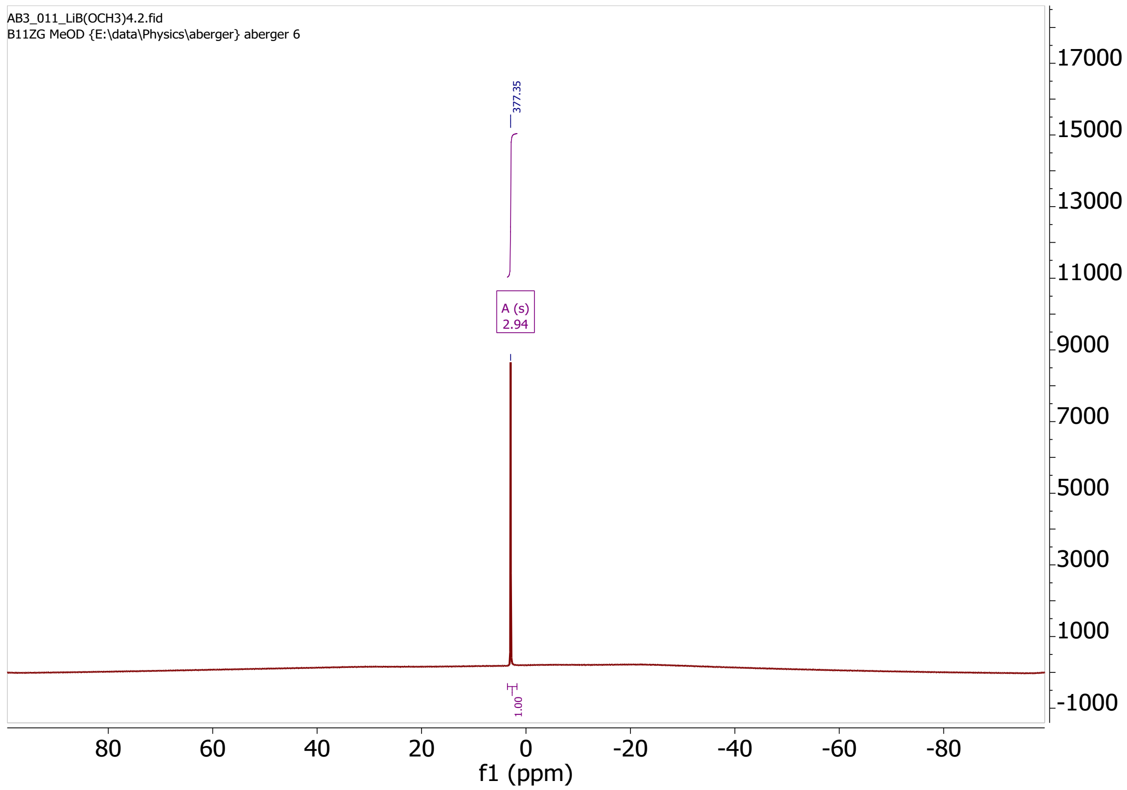

Figure S15: $^{11}B$ NMR of $Li[B(OMe)_4]$ in MeOD.

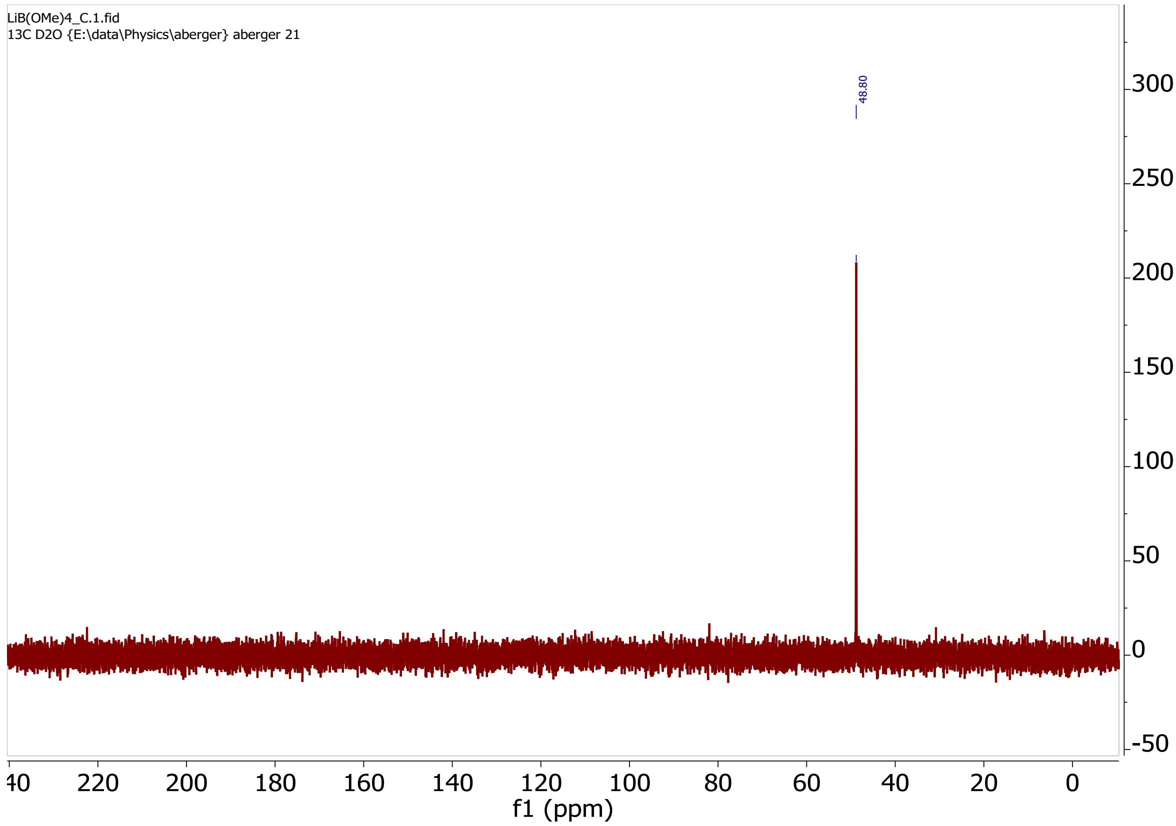


Figure S16: $^{13}C\{^1H\}$ NMR of $Li[B(OMe)_4]$ in $D_2O$.

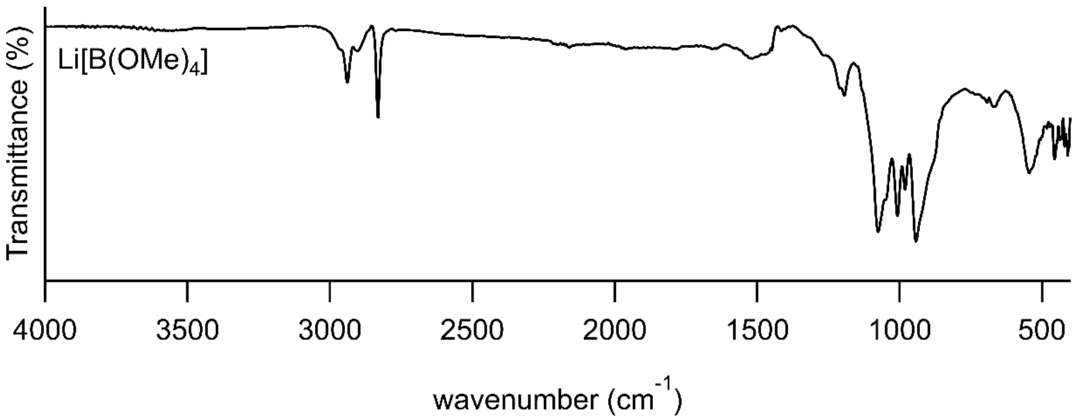


Figure S17: FTIR of $Li[B(OMe)_4]$.

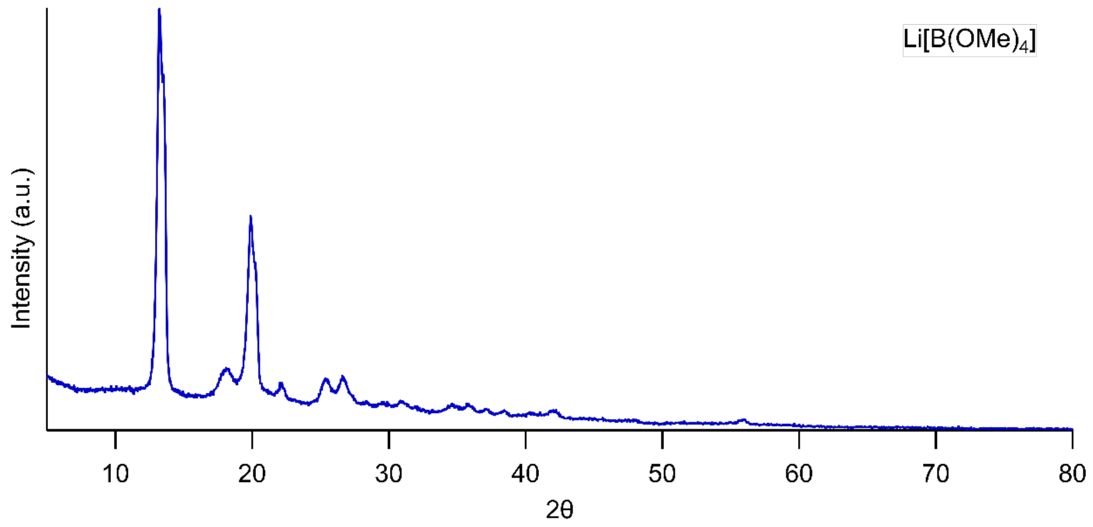


Figure S18: XRD of Li[B(OMe)$_4$]. CuKα radiation, 1.54056 Å.

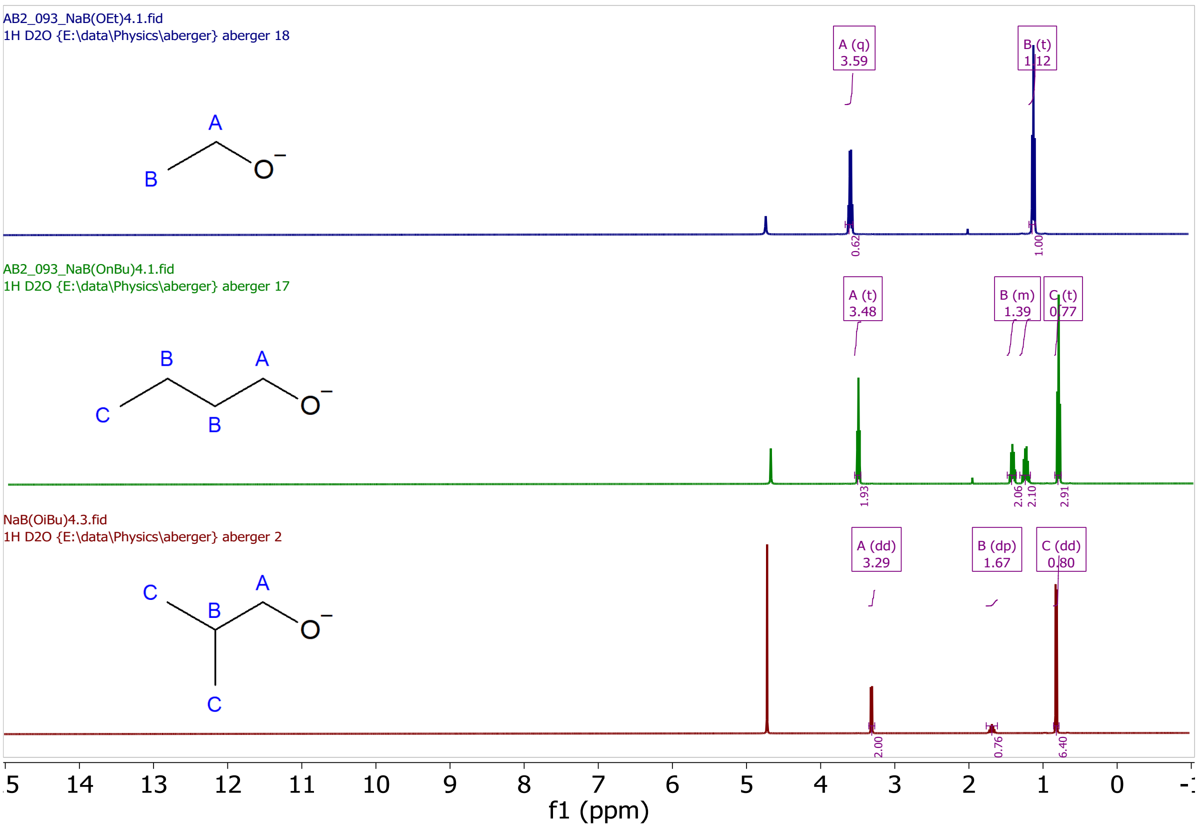


Figure S19: $^1$H NMR of Na[B(OEt)$_4$] (top), Na[B(OBu)$_4$] (middle) and Na[B(O$^i$Bu)$_4$] in $D_2O$.

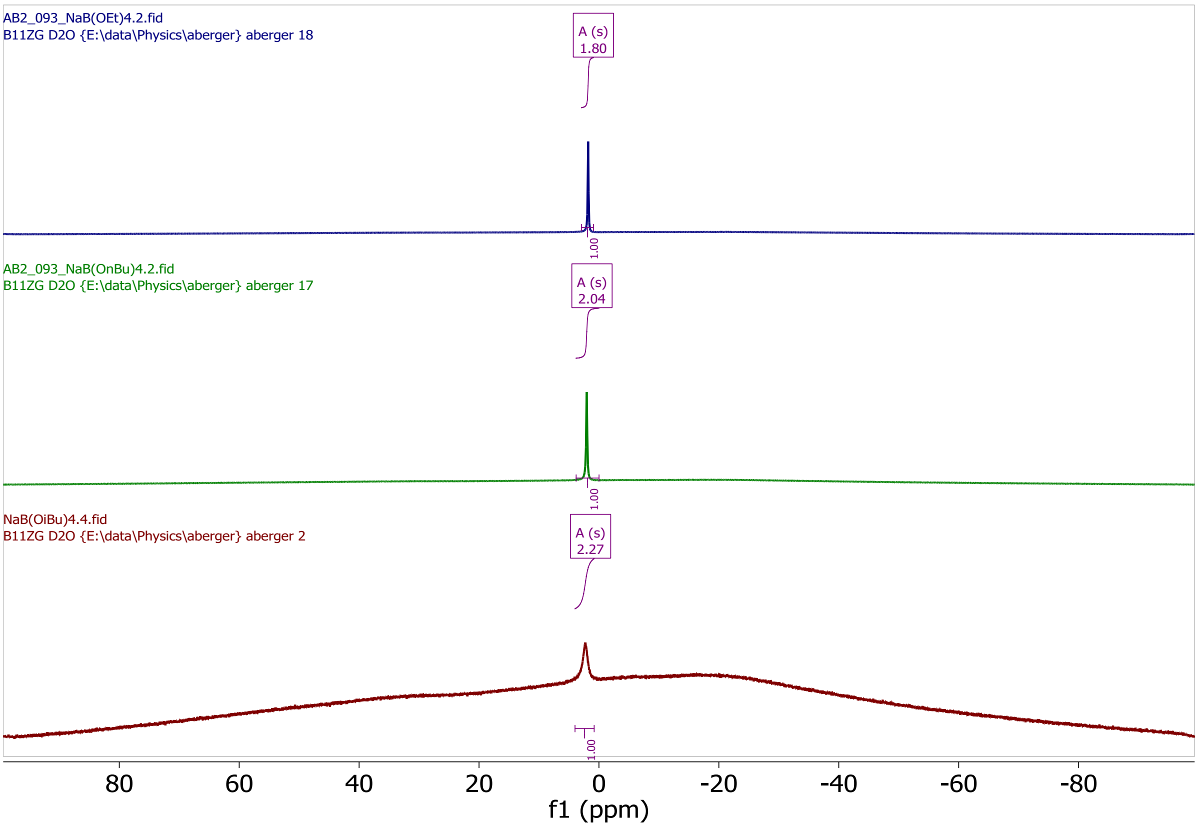


Figure S20: $^{11}$B NMR of $Na[B(OEt)_4]$ (top), $Na[B(OBu)_4]$ (middle) and $Na[B(O^iBu)_4]$ in $D_2O$.

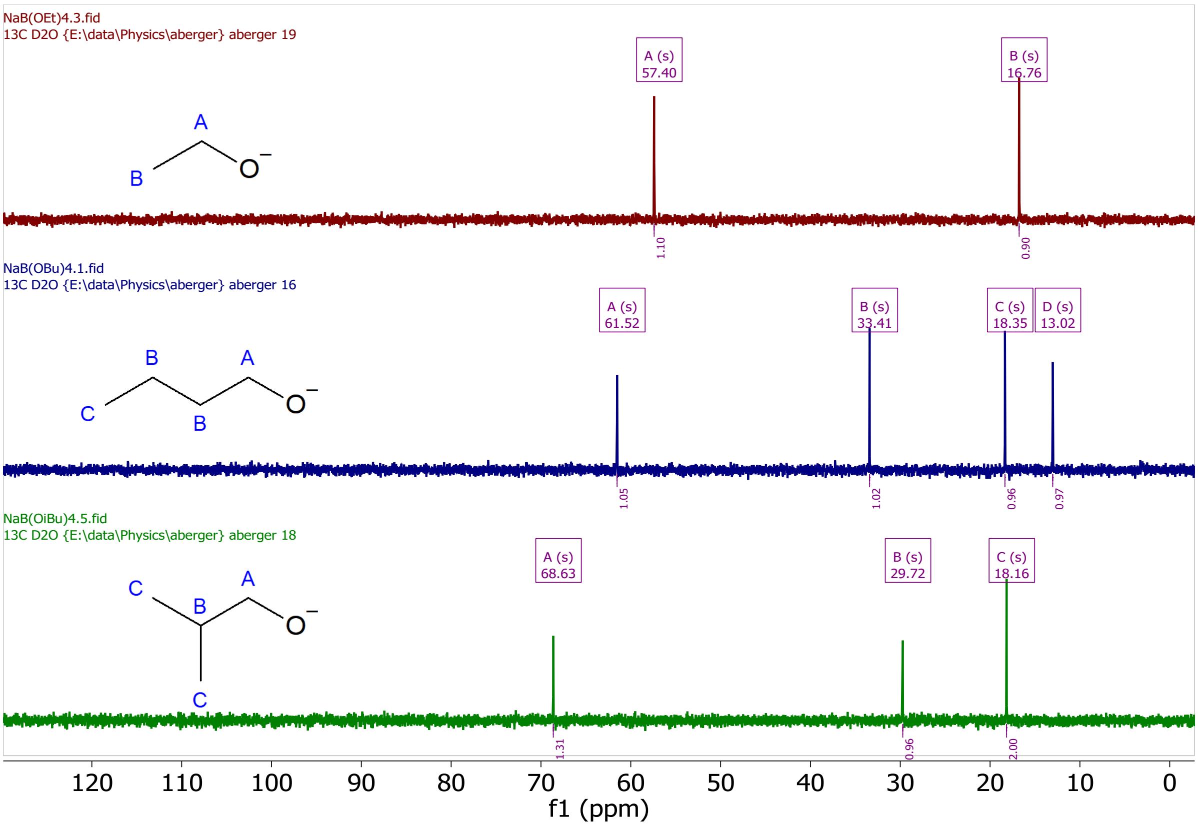


Figure S21: $^{13}C\{^1H\}$ NMR of $Na[B(OEt)_4]$ (top), $Na[B(OBu)_4]$ (middle) and $Na[B(O^iBu)_4]$ in $D_2O$.

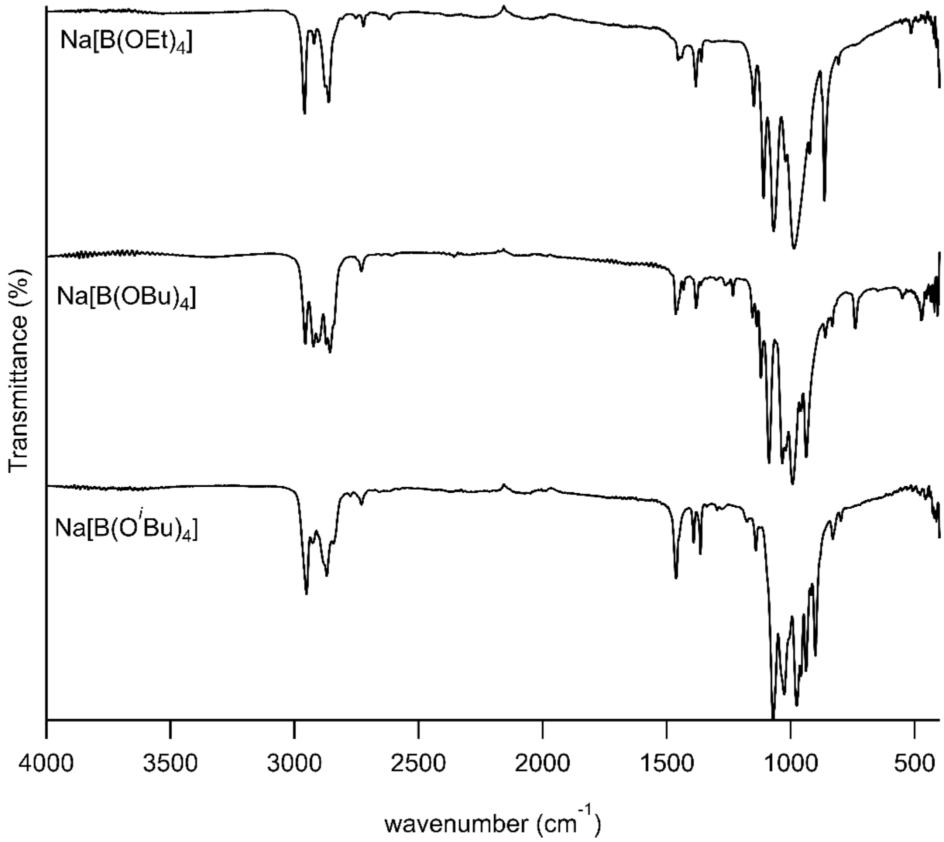


Figure S22: FTIR of Na[B(OEt)$_4$] (top), Na[B(OBu)$_4$] (middle) and Na[B(O$^i$Bu)$_4$] (bottom).

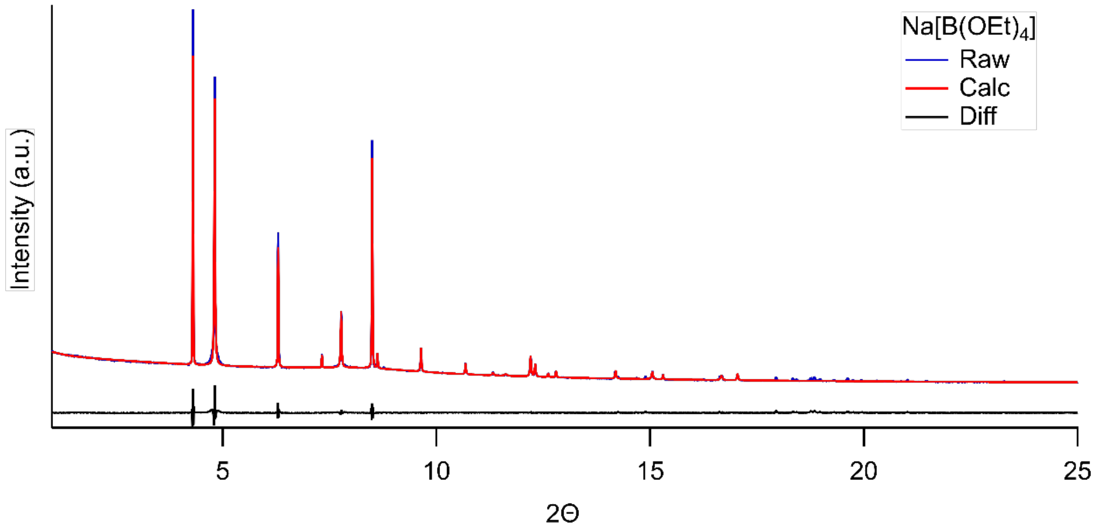


Figure S23: SR-XRD pattern for Na[B(OEt)$_4$] at room temperature. Indexed in orthorhombic space group I222 ($a$ = 15.7169(4) Å, $b$ = 7.8587(1) Å, $c$ = 5.7196(1) Å, $V$ = 706.47(2) Å$^3$), $\lambda$ = 0.590888(2) Å.

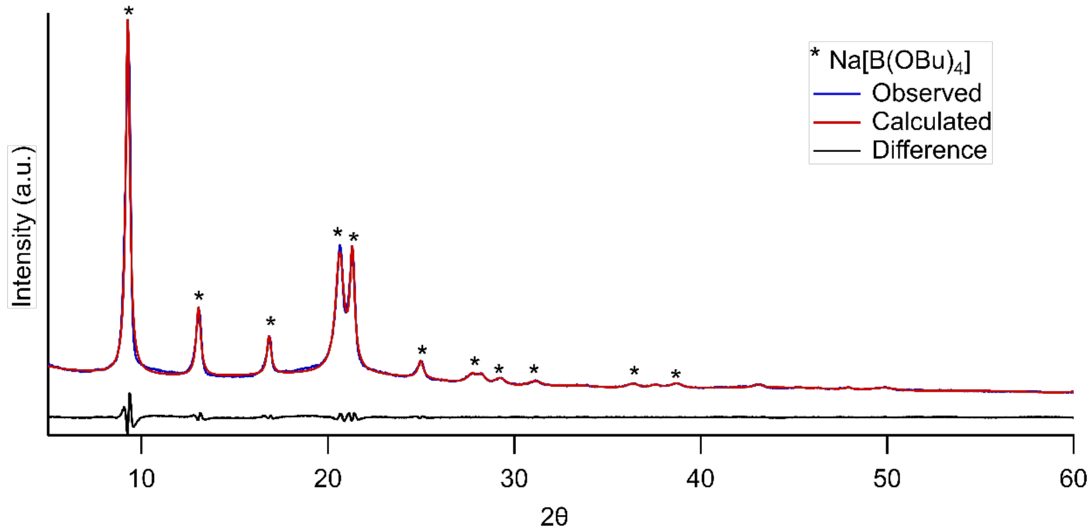


Figure S24: XRD Pattern for $Na[B(OBu)_4]$. CuKα radiation, 1.54056 Å. * indicates the known peaks for $Na[B(OBu)_4]$.

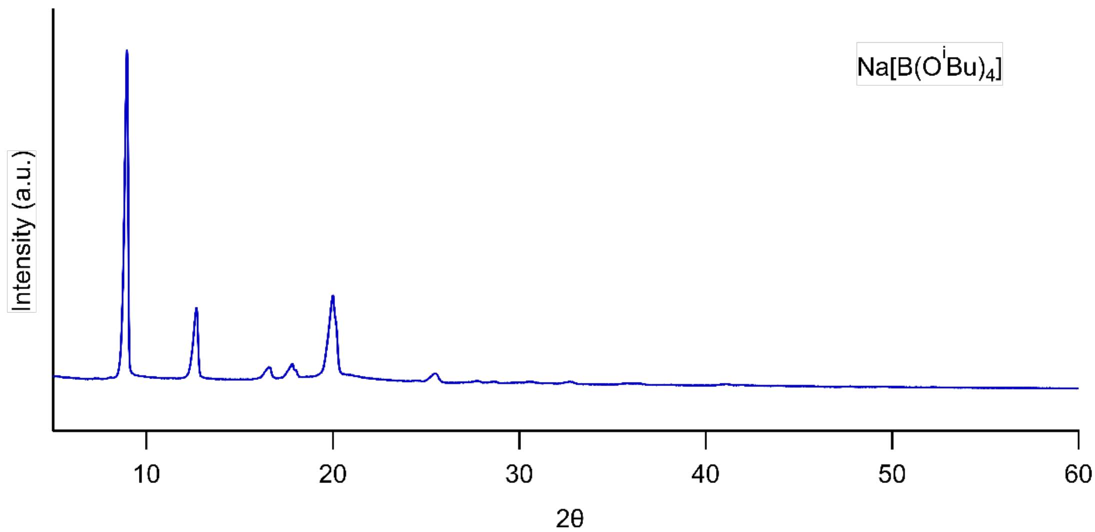


Figure S25: XRD Pattern for $Na[B(O^iBu)_4]$. CuKα radiation, 1.54056 Å.

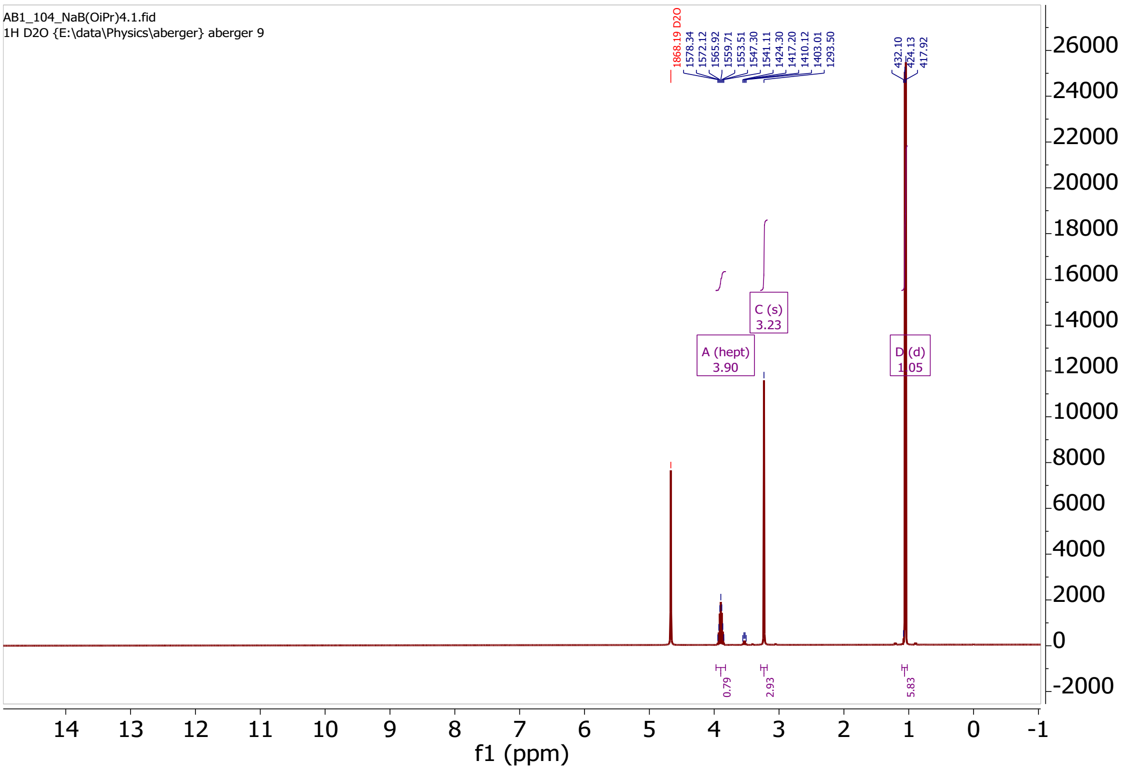


Figure S26: $^{1}H$ NMR of $Na[B(OMe)_x(O^iPr)_{4-x}]$ in $D_2O$ synthesised using the transesterification method.

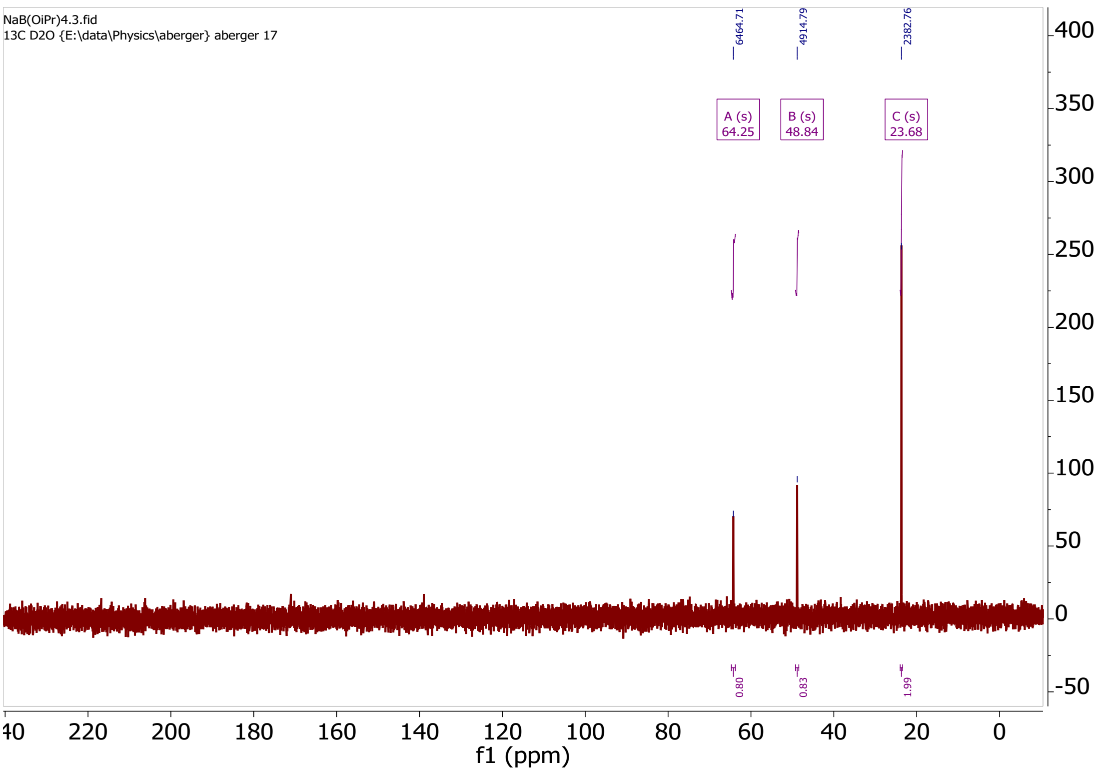


Figure S27: $^{13}C$ NMR of $Na[B(OMe)_x(O^iPr)_{4-x}]$ in $D_2O$ synthesised using the transesterification method.

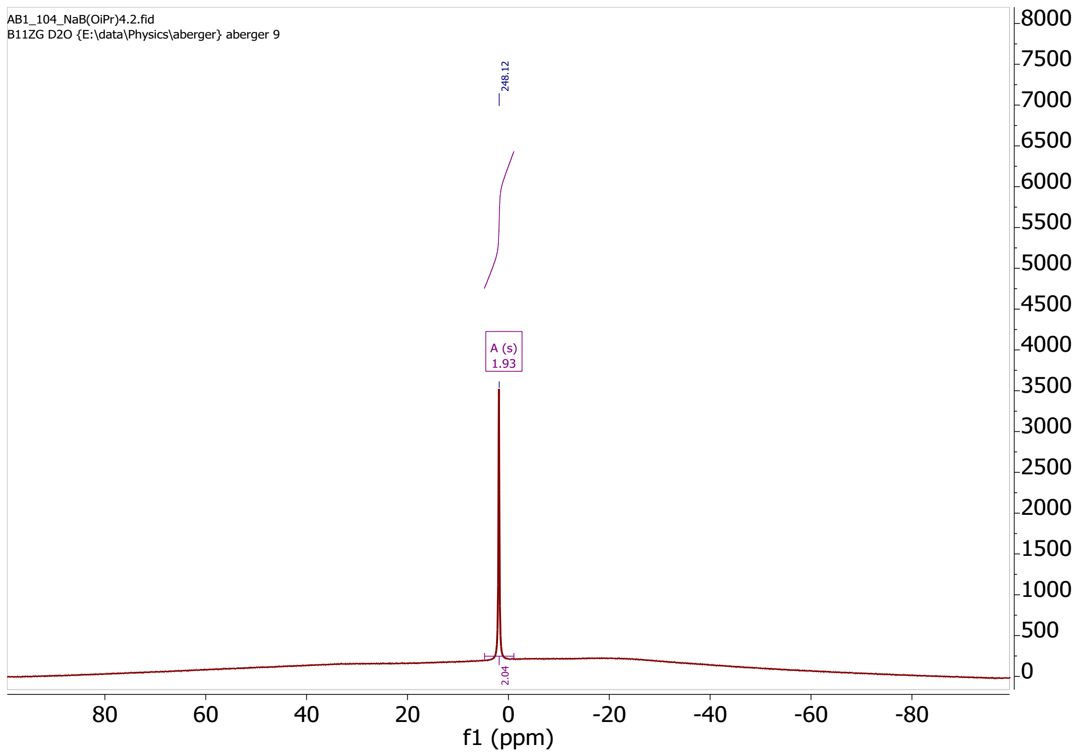


Figure S28: $^{11}B$ NMR of $Na[B(OMe)_x(O^iPr)_{4-x}]$in $D_2O$ synthesised using the transesterification method.

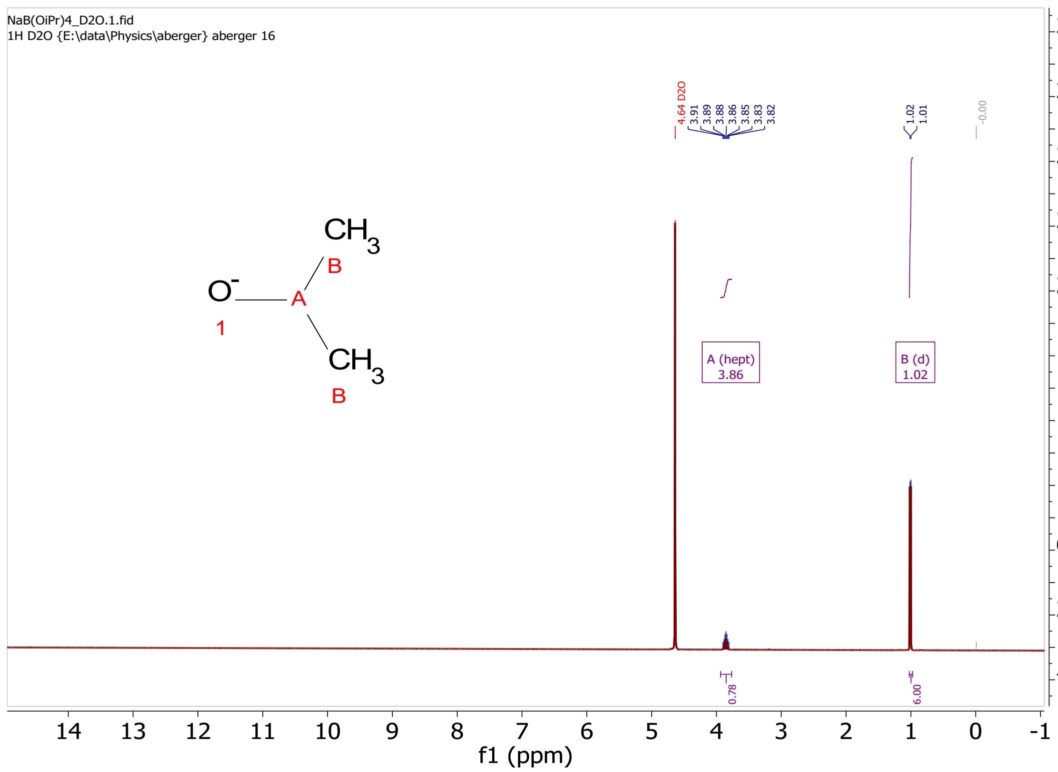


Figure S29: $^1H$ NMR of $Na[B(O^iPr)_4]$ in $D_2O$.

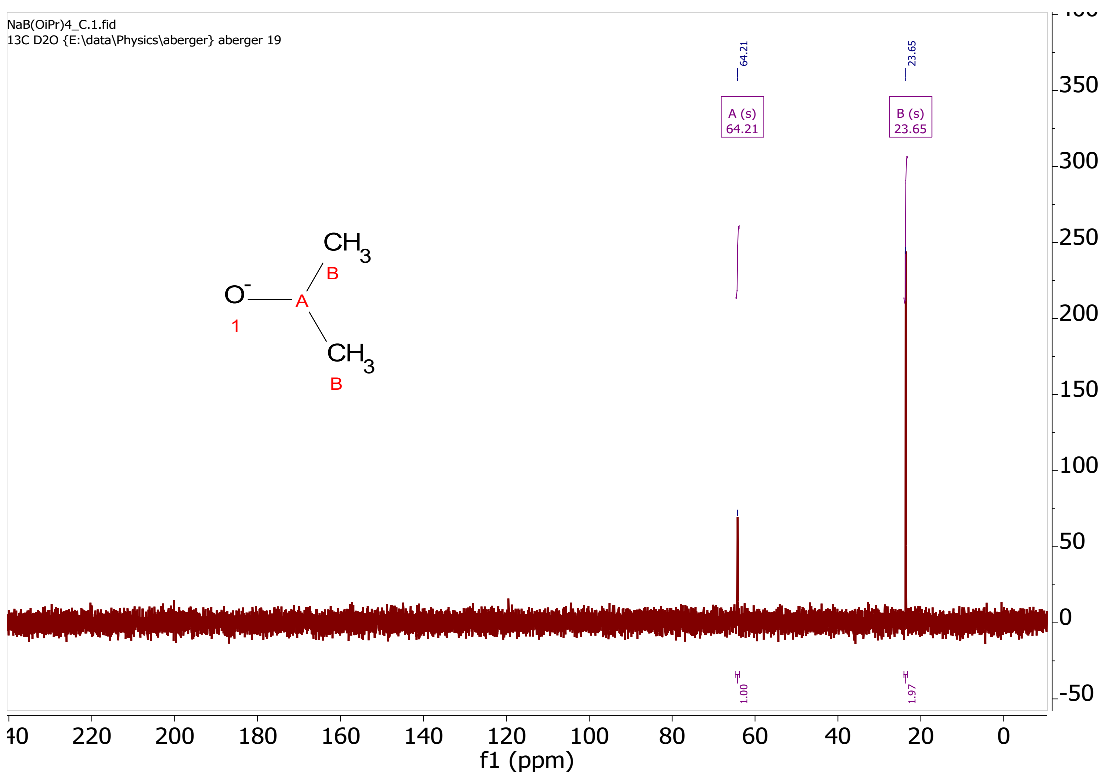


Figure S30: $^{13}C\{^{1}H\}$ NMR of $Na[B(O^{i}Pr)_4]$ in $D_2O$.

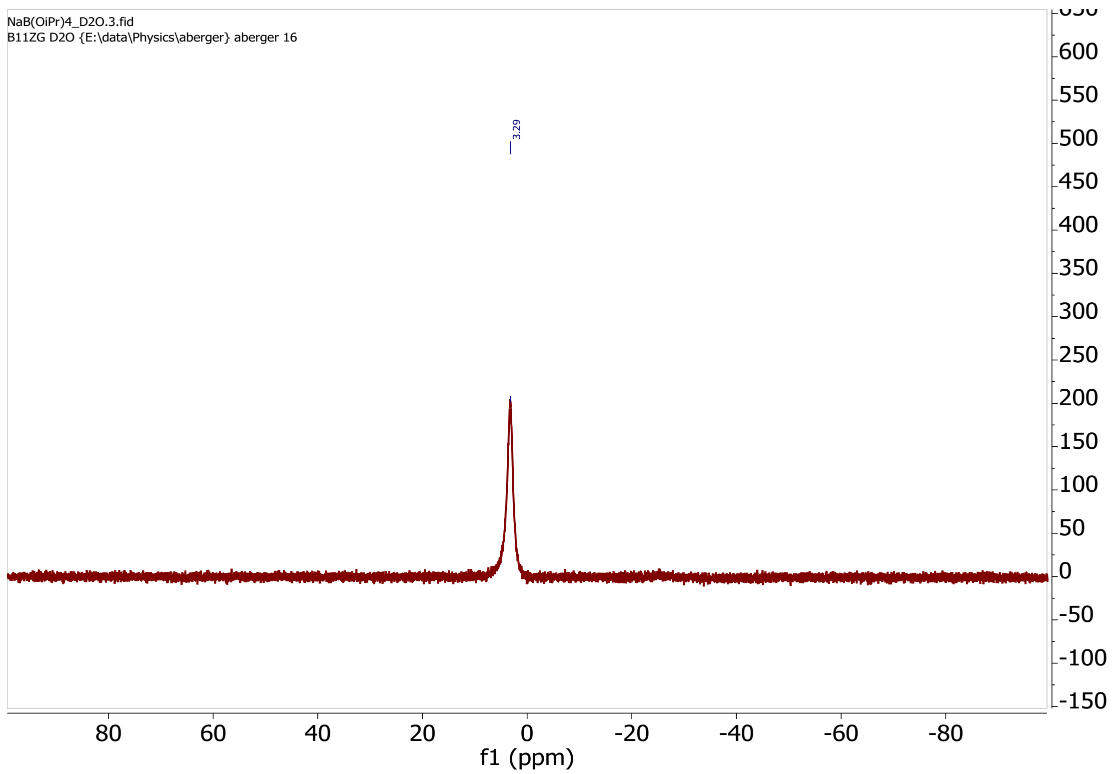


Figure S31: $^{11}B$ NMR of $Na[B(O^{i}Pr)_4]$ in $D_2O$.

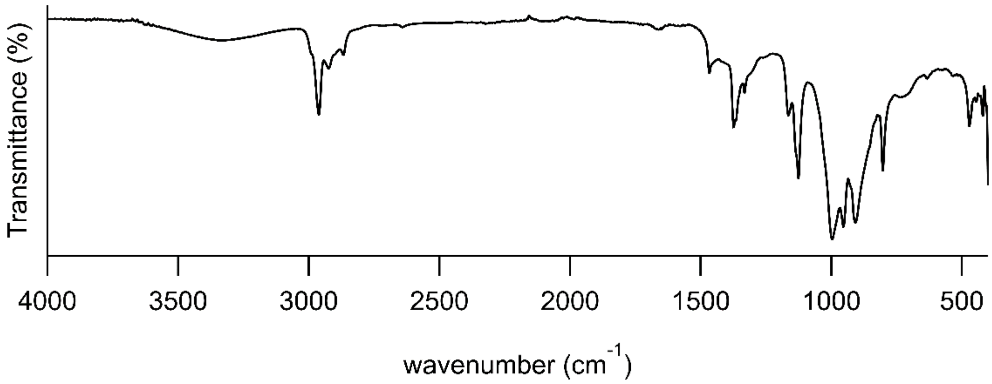


Figure S32: FTIR of Na[B(O$^i$Pr)$_4$].

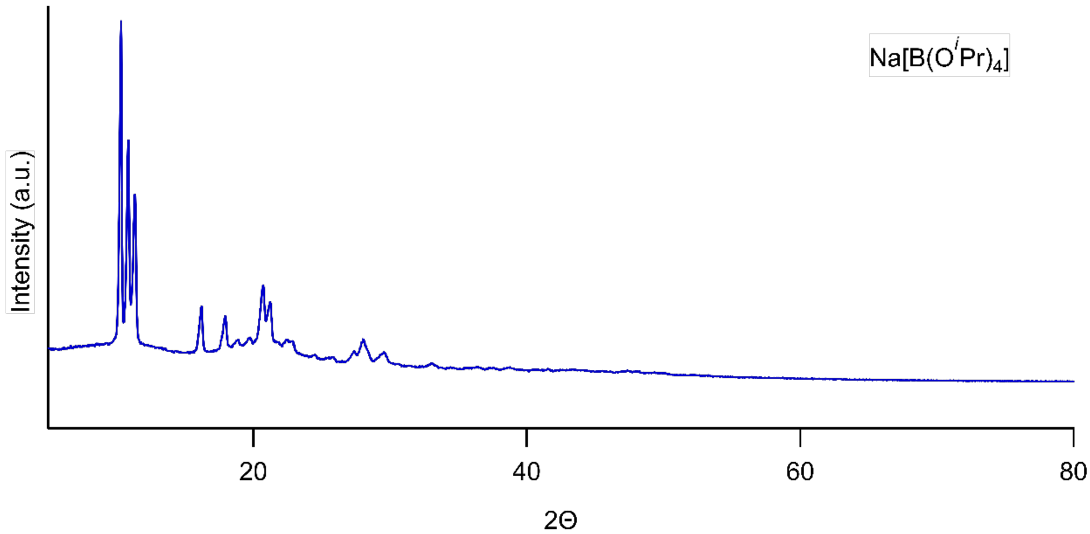


Figure S33: XRD of Na[B(O$^i$Pr)$_4$]. CuKα radiation, 1.54056 Å.

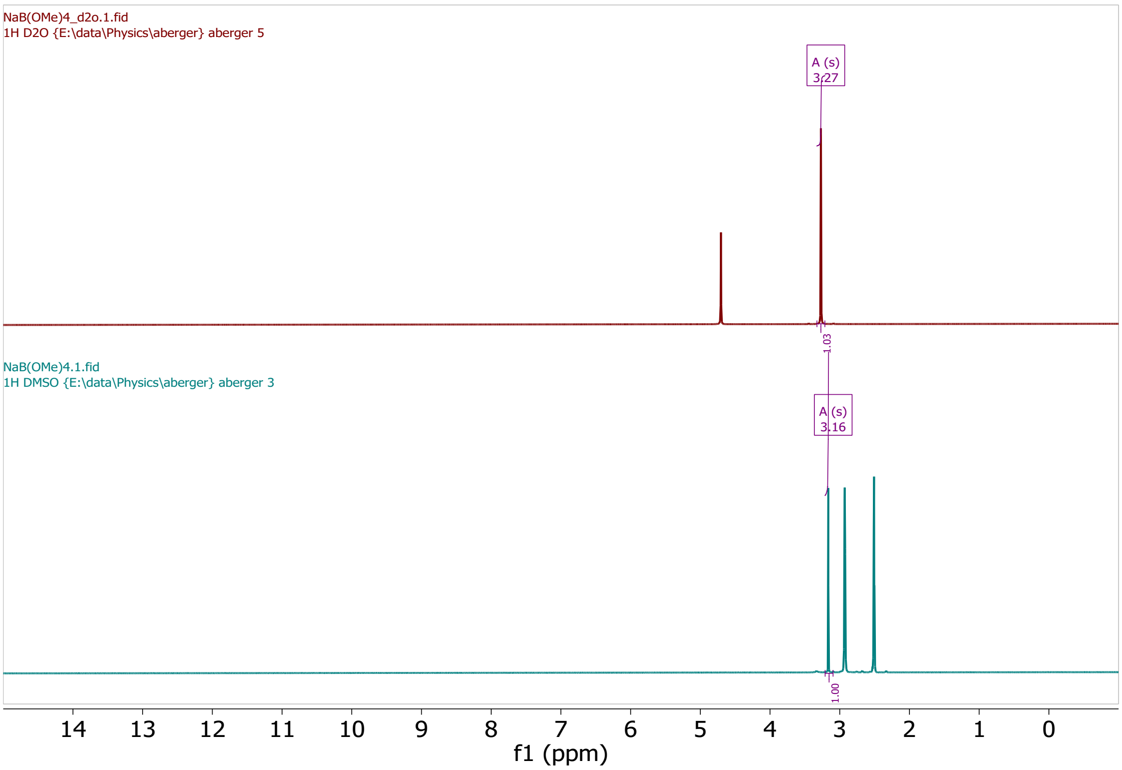


Figure S34: $^{1}H$ NMR of $Na[B(OMe)_4]$ in $D_2O$ (top) and DMSO-*d6* (bottom).

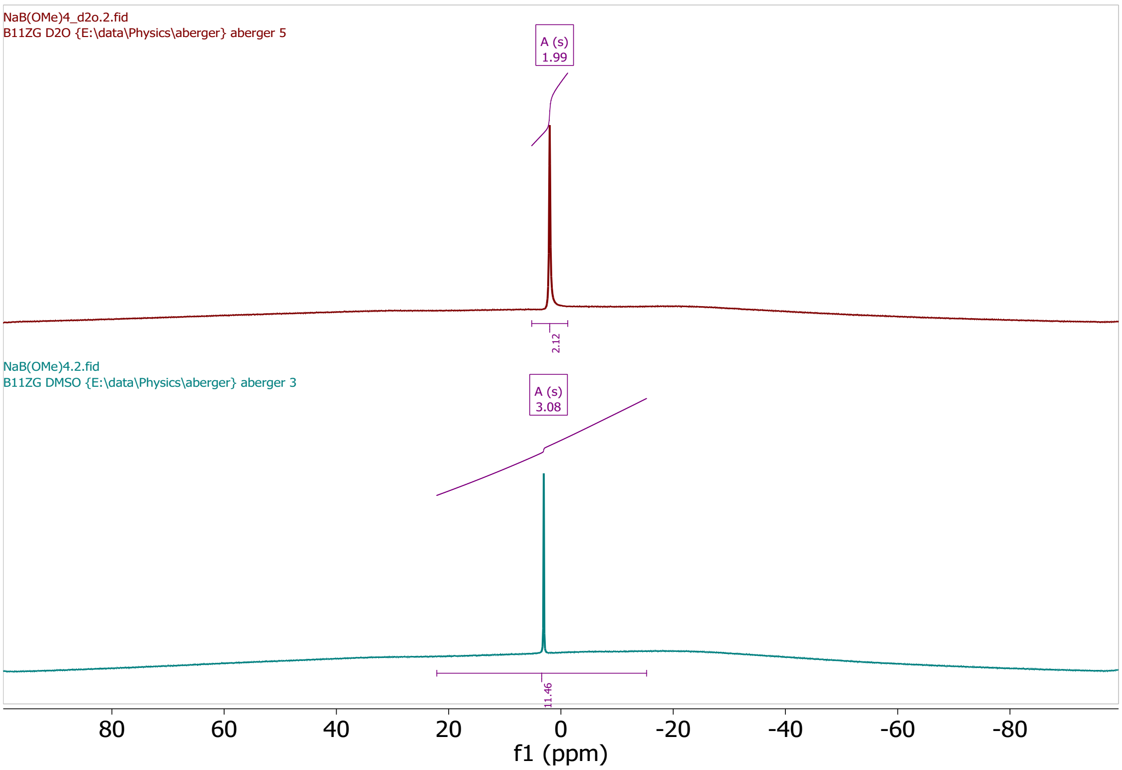


Figure S35: $^{11}B$ NMR of $Na[B(OMe)_4]$ in $D_2O$ (top) and DMSO-*d6* (bottom).

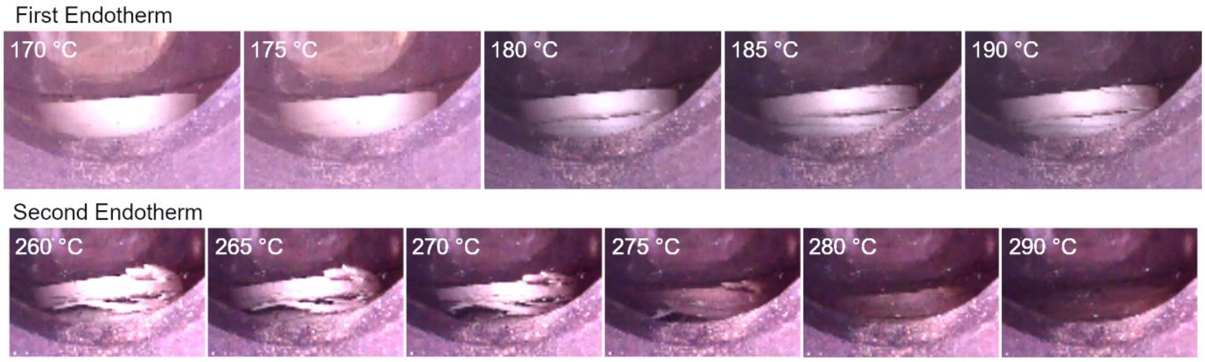


Figure S36: TPPA of Na[B(OMe)$_4$] indicating the phase change occurring between 170 - 190 °C (the first endotherm indicated by DSC) and the decomposition of Na[B(OMe)$_4$] (the second endotherm in DSC). Heat ramp was performed at 4 °C/min under argon.

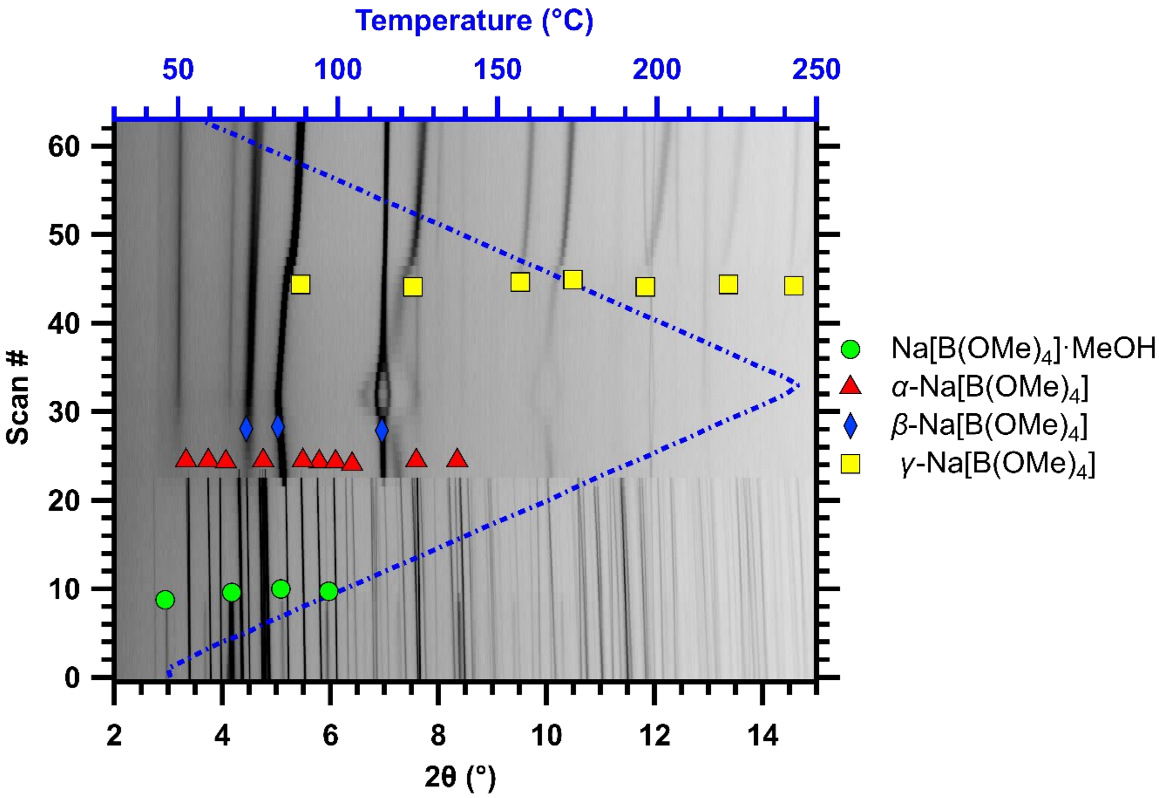


Figure S37: *In situ* SR-XRD ramp and cool of Na[B(OMe)$_4$]. ($\lambda$ = 0.590888(2) Å, heating $\Delta T/\Delta t$ = 5 °C min$^{-1}$).

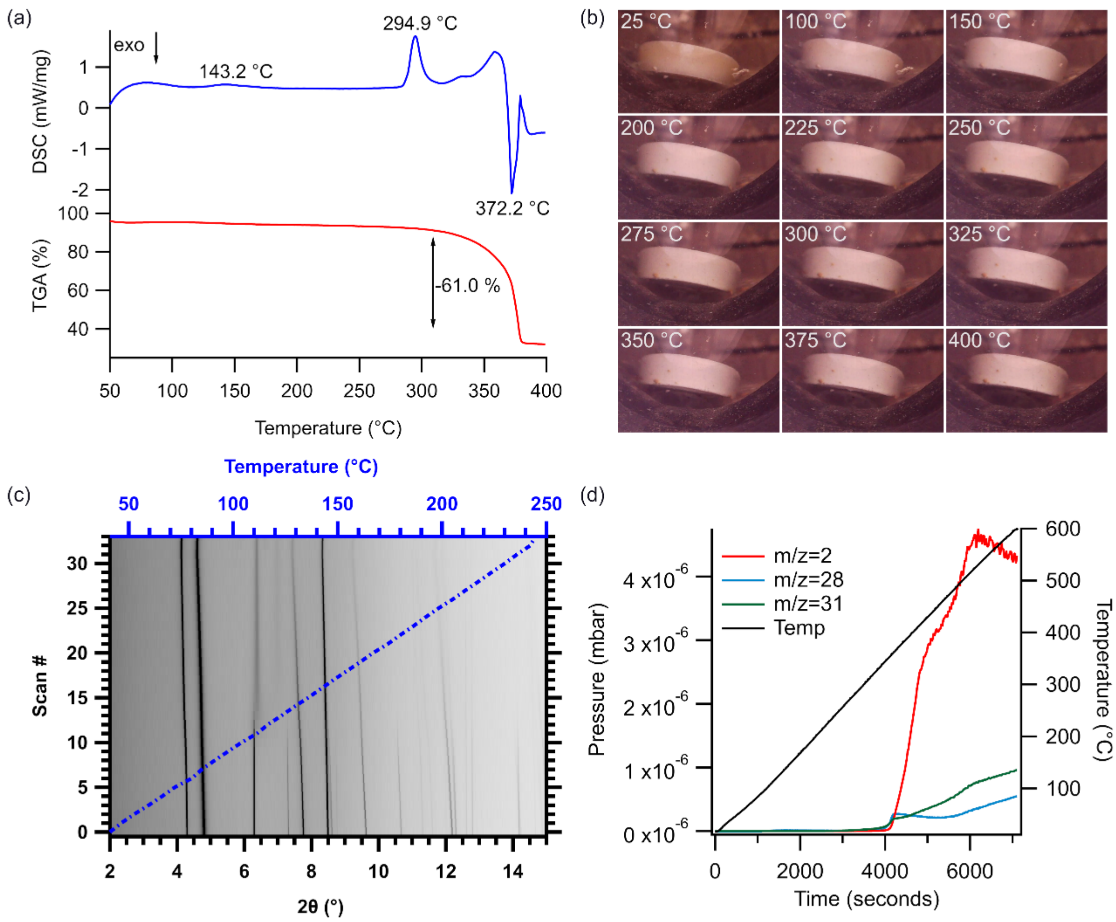


Figure S38: Thermal analysis of $Na[B(OEt)_4]$ using (a) DSC-TGA (5.52 mg), (b) TPPA, (c) SR-XRD ($\lambda$ = 0.590888(2) Å, heating $\Delta T/\Delta t$ = 5 °C min$^{-1}$)., and (d) RGA-MS. DSC-TGA was analysed with a 20 °C/min ramp rate and Ar flow of 40 mL/min. TPPA had a ramp rate of 4 °C/min under Ar atmosphere and a pellet thickness of 1.90 mm. RGA-MS was run from 25 °C to 600 °C with a scan range for RGA-MS was 1 - 100 amu under a vacuum pressure of approximately $10^{-3}$ - $10^{-4}$ mbar.

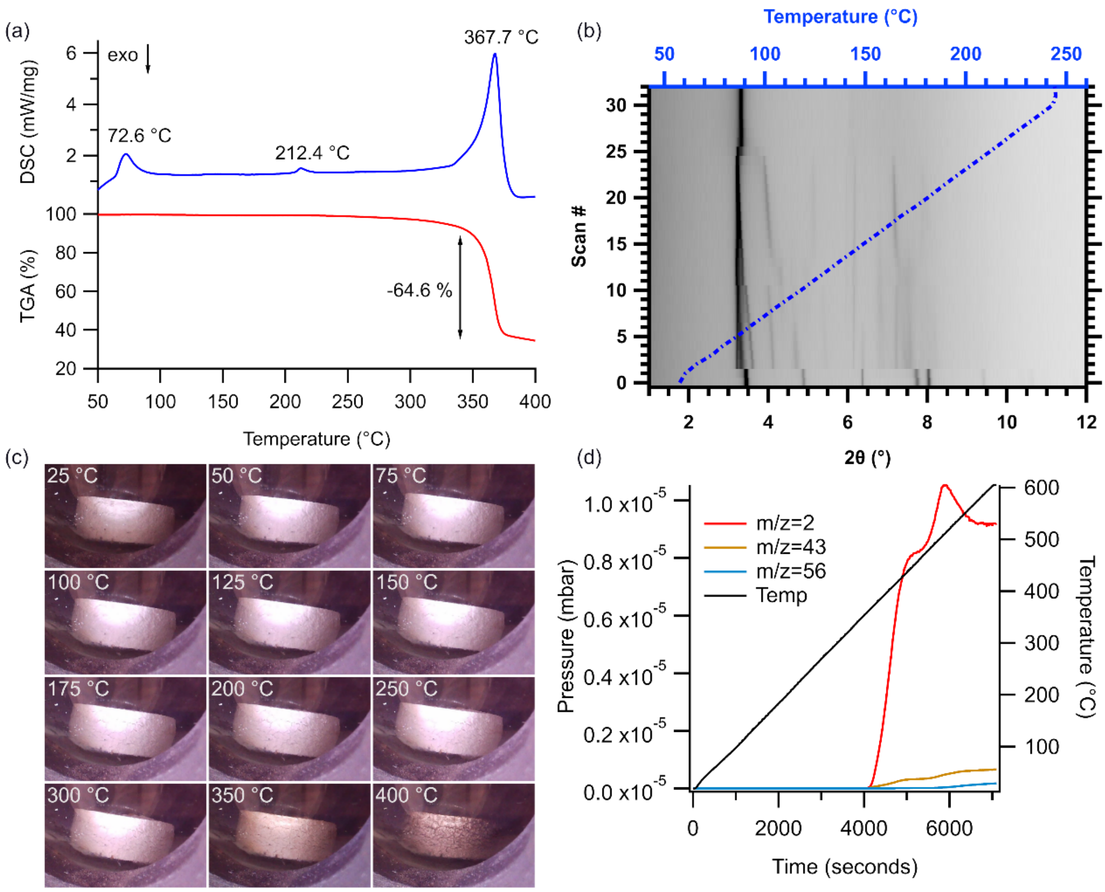


Figure S39: Thermal analysis of Na[B(OBu)$_4$] using (a) DSC-TGA (6.47 mg), (b) TPPA, (c) SR-XRD ($\lambda$ = 0.590888(2) Å, heating $\Delta T/\Delta t$ = 5 °C min$^{-1}$), and (d) RGA-MS. DSC-TGA was analysed with a 20 °C/min ramp rate and Ar flow of 40 mL/min. TPPA had a ramp rate of 4 °C/min under Ar atmosphere and a pellet thickness of 2.27 mm. RGA-MS was run from 25 °C to 600 °C with a scan range for RGA-MS was 1 - 100 amu under a vacuum pressure of approximately $10^{-3}$ - $10^{-4}$ mbar

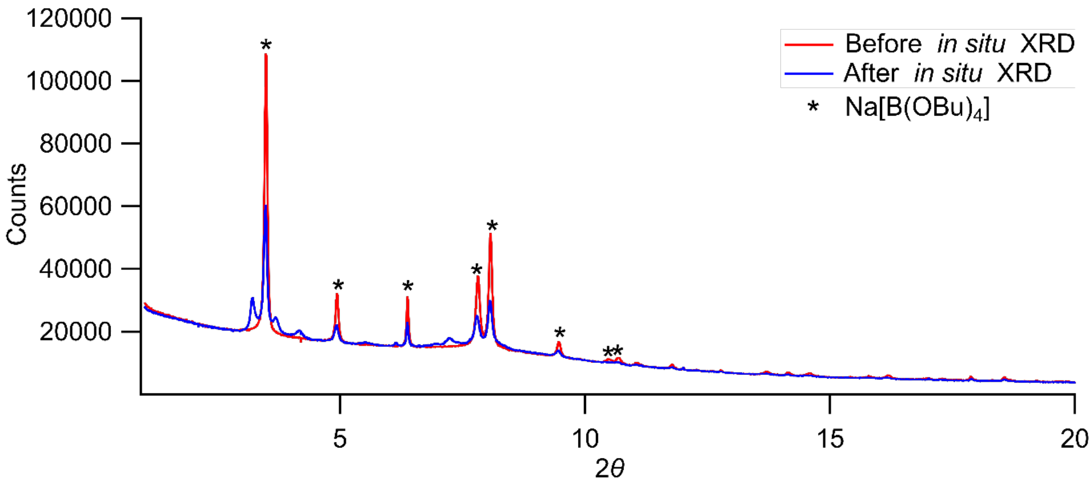


Figure S40: Room temperature SR-XRD patterns of Na[B(OBu)$_4$] from before *in situ* analysis (red) and at room temperature after heating to 240 °C (blue). $\lambda$ = 0.590888(2) Å.

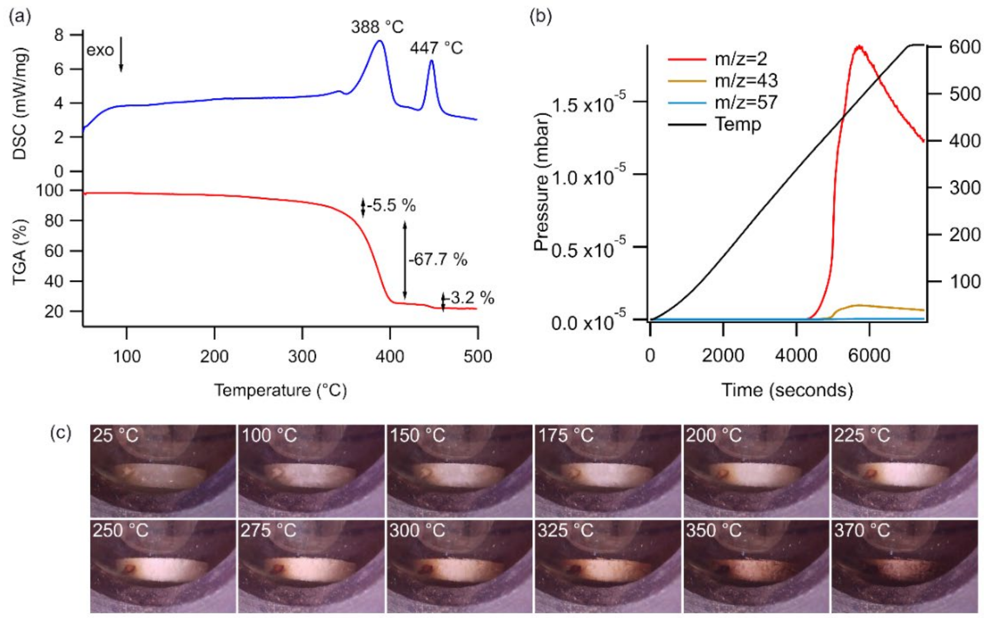


Figure S41: Thermal analysis of Na[B(O$^i$Bu)$_4$] using (a) DSC-TGA (6.47 mg), (b) RGA-MS and (c) TPPA. DSC-TGA was analysed with a 20 °C/min ramp rate and Ar flow of 40 mL/min. RGA-MS was run from 25 °C to 600 °C with a scan range for RGA-MS was 1 - 100 amu under a vacuum pressure of approximately $10^{-3}$ - $10^{-4}$ mbar. TPPA had a ramp rate of 4 °C/min under Ar atmosphere and a pellet thickness of 1.59 mm. Small fragment is a contaminant not sample.

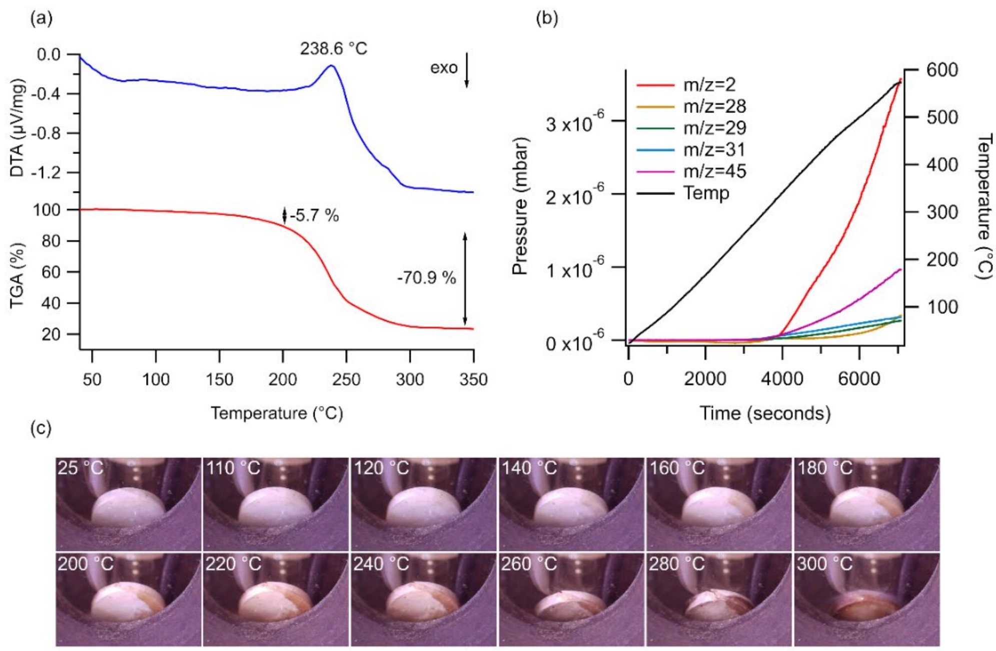


Figure S42: Thermal analysis of Na[B(O$^i$Pr)$_4$] using (a) DTA-TGA, (b) RGA-MS and (c) TPPA. DTA-TGA was analysed with a 10 °C/min ramp rate and Ar flow of 40 mL/min. RGA-MS was run from 25 °C to 600 °C with a scan range for RGA-MS was 1 - 100 amu under a vacuum pressure of approximately $10^{-3}$ - $10^{-4}$ mbar. TPPA had a ramp rate of 4 °C/min under Ar atmosphere and a pellet thickness of 1.05 mm.

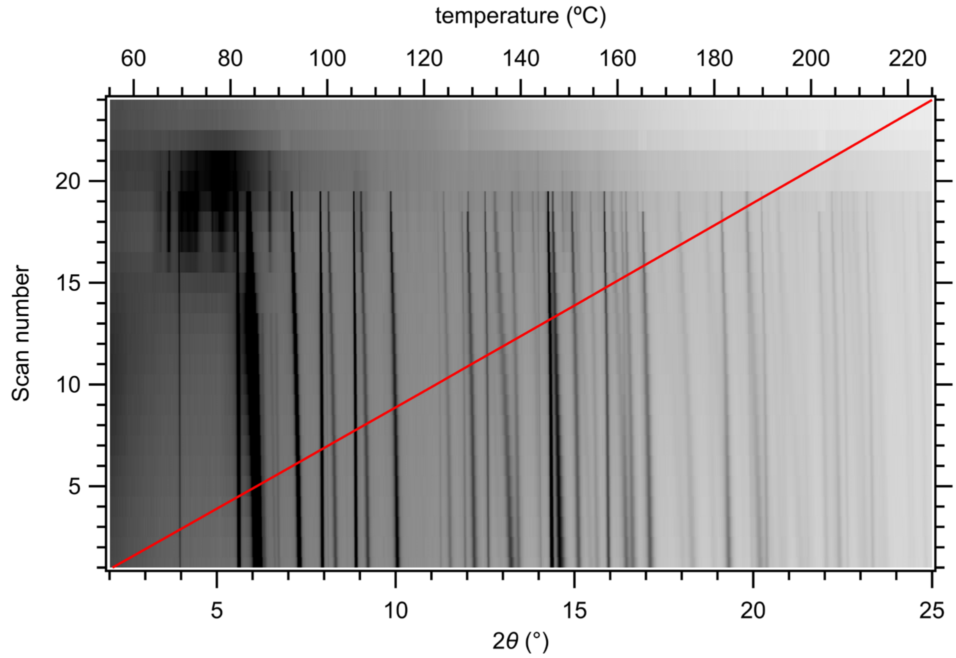


Figure S43: Thermal analysis of K[B(OMe)$_4$] using SR-XRD ($\lambda$ = 0.774993(1) Å, heating $\Delta T/\Delta t$ = 6 °C min$^{-1}$).

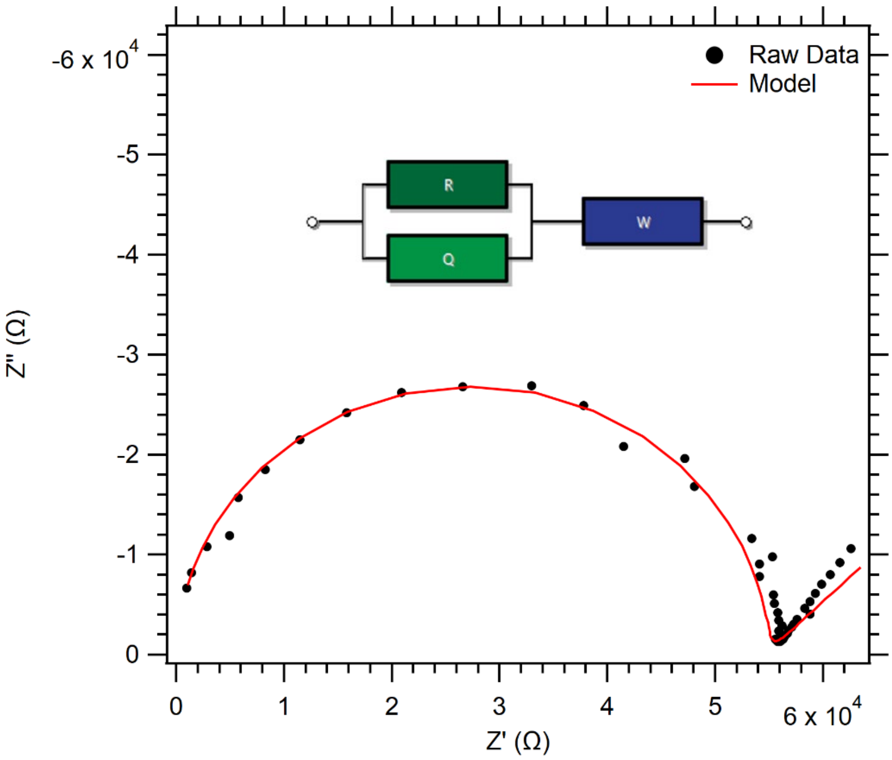


Figure S44: Nyquist impedance plot of K[B(OMe)$_4$] at 135°C showing fit to data using an equivalent circuit to determine the *x*-intercept of the Nyquist semicircle. *Q*, *R*, and *W* refer to constant phase element, resistor, and open circuit Warburg element, respectively.

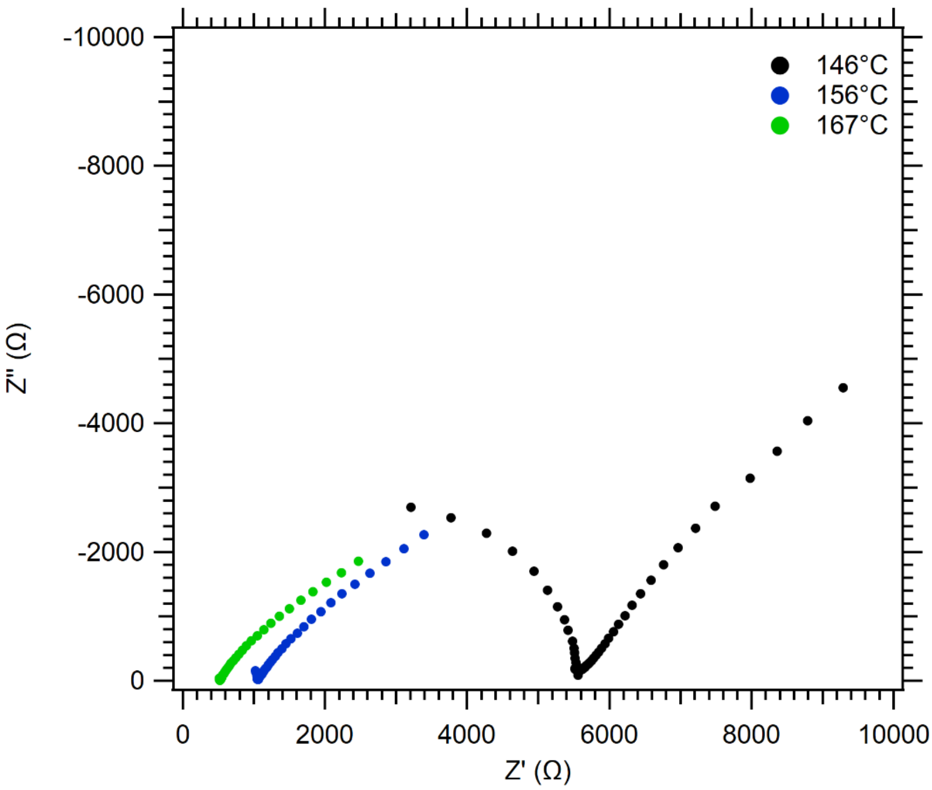


Figure S45: Nyquist impedance plot of K[B(OMe)$_4$] at various temperatures showing ionic Warburg low frequency spikes.

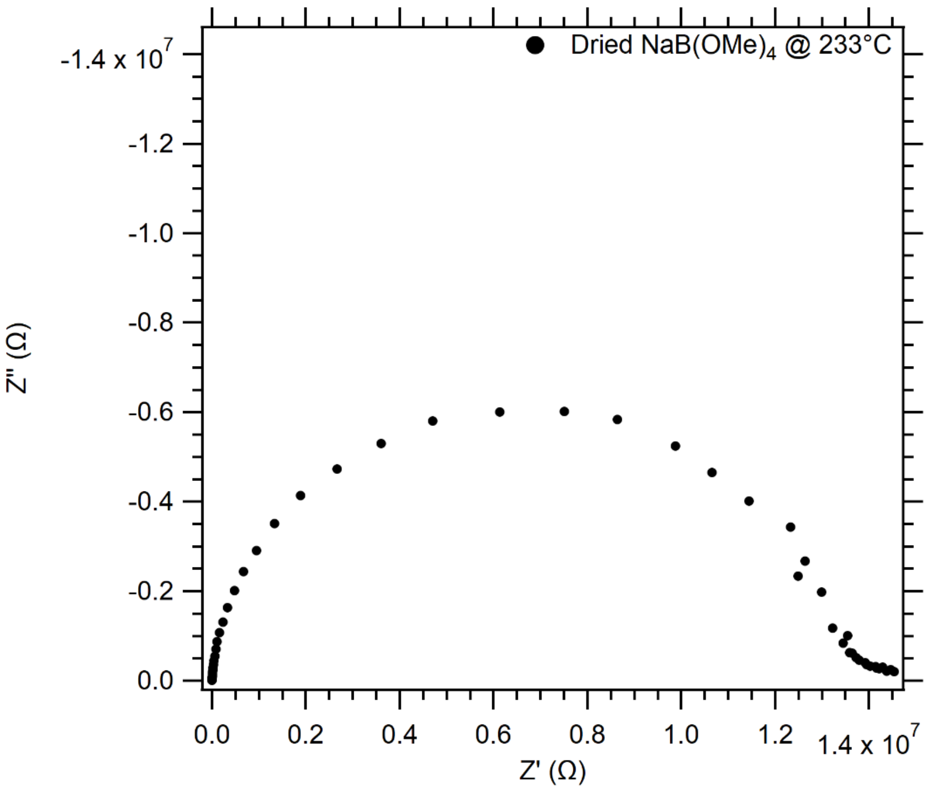


Figure S46: Nyquist impedance plot of dried Na[B(OMe)$_4$] at 233°C.

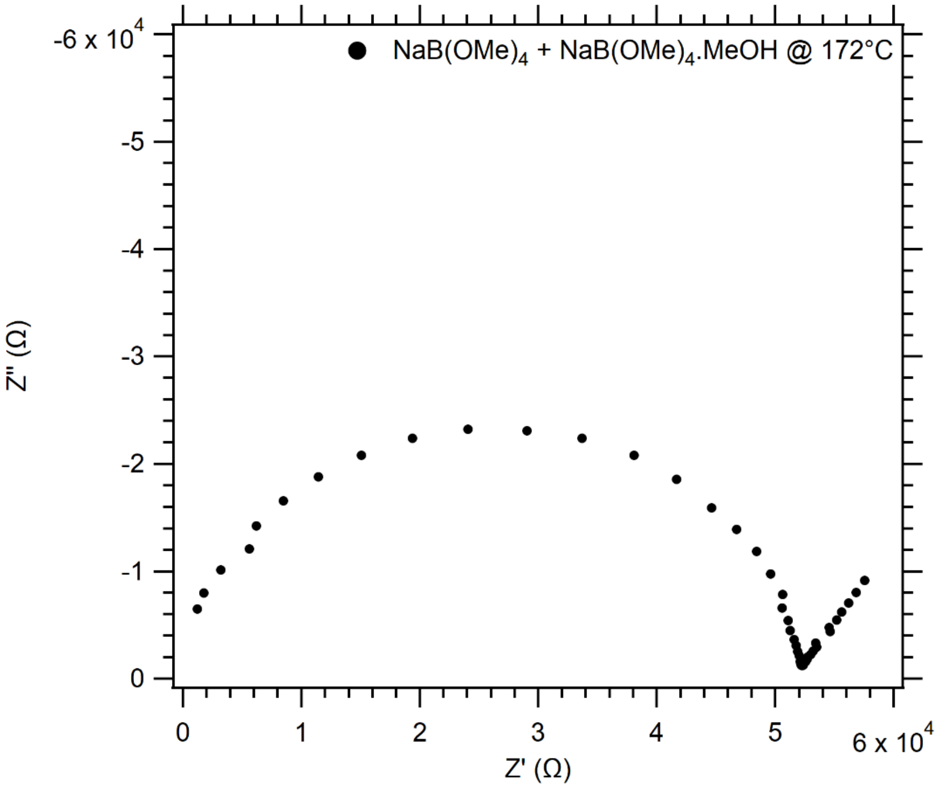


Figure S47: Nyquist impedance plot of Na[B(OMe)$_4$] + Na[B(OMe)$_4$].MeOH at 172°C.

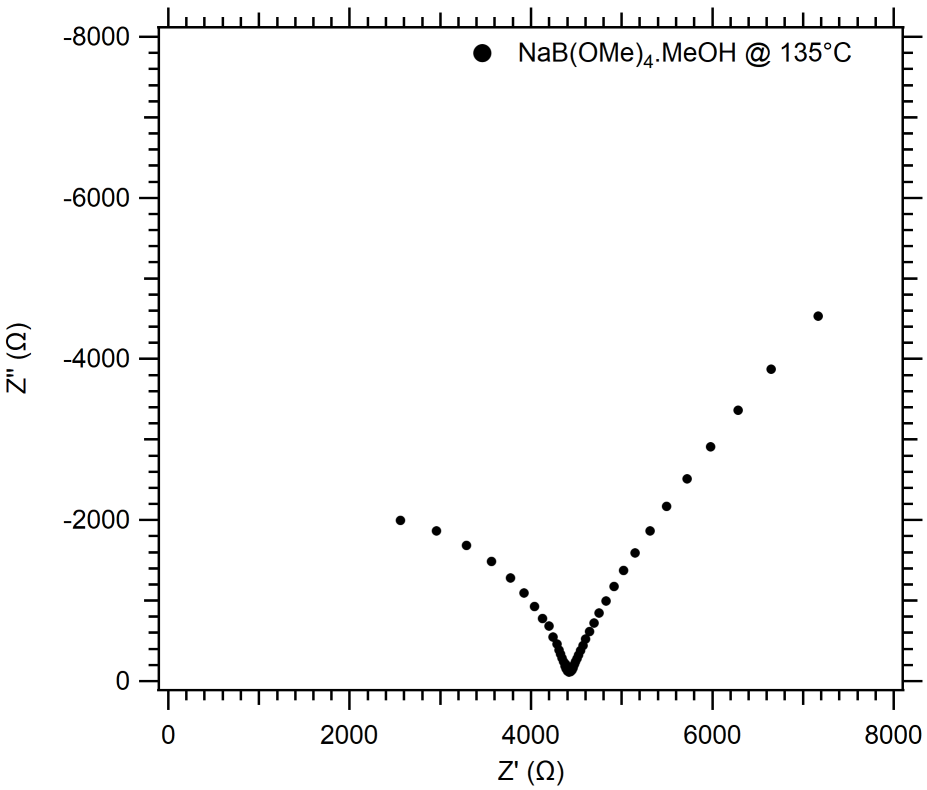


Figure S48: Nyquist impedance plot of Na[B(OMe)$_4$].MeOH at 135°C.